Non-equilibrium development in turbulent boundary layers with changing pressure gradients

Ralph J. Volino†

Mechanical Engineering Department, United States Naval Academy, Annapolis, MD 21402, USA

Turbulence measurements were made in smooth-wall boundary layers subject to changing pressure gradients. Cases were documented over a range of Reynolds numbers and acceleration parameters. In all cases the boundary layer was subject to an initial zero pressure gradient (ZPG) development, followed by a favourable pressure gradient (FPG), a ZPG recovery and an adverse pressure gradient (APG). In the non-ZPG regions, the acceleration parameter, K, was held constant. Two component velocity profiles were acquired at multiple streamwise locations to document the response to the changing pressure gradient of the mean velocity, Reynolds stresses and triple products of the fluctuating velocity components. Velocity field measurements were made to document the turbulence structure using two point correlations. In general, turbulence was suppressed by the FPG while structures became larger in streamwise and spanwise extent relative to the boundary layer thickness, particularly near the wall. In the recovery region, the return to canonical ZPG conditions was rapid. Changes in the structure in the APG region were less pronounced. The changes in the turbulence statistics and correlations relative to the ZPG baseline were quantified and presented as functions of streamwise location. When the streamwise location is scaled using the acceleration parameter, the results from all cases (including all statistical moments, and the size and inclination angles of turbulence structures), collapse in each region of the flow, showing a common non-equilibrium response to changes in the pressure gradient. These are new results which apply to the present flows and those with similar types of pressure gradients, but are not necessarily applicable to all flows with arbitrary pressure gradients.

Key words: turbulent boundary layers, boundary layer structure

1. Introduction

Turbulent boundary layers have been well studied, and the understanding of their behaviour has steadily advanced with the development of new and higher fidelity measurement techniques and the advent of computational tools for direct numerical simulation (DNS). Mean velocity profiles, turbulence statistics, and wall

† Email address for correspondence: volino@usna.edu

shear have been documented over a large range of Reynolds numbers. Velocity field measurements have shown the role of structures such as hairpin packets and larger scale motions in determining the mean flow behaviour. Measurements and computations have focused mainly, although certainly not exclusively, on the canonical, flat, smooth-wall, zero pressure gradient (ZPG) case. Reviews of ZPG studies include Fernholz & Finley (1996) and Klewicki (2010). Recent examples of experiments in the literature include Vincenti *et al.* (2013) and Samie *et al.* (2018). Computational studies include Jiménez *et al.* (2010) and Sillero, Jiménez & Moser (2013). The ZPG case was the logical choice to start building the understanding of turbulent boundary layers since in many ways it is the simplest case, at least in terms of complicating effects, if not flow structure. The ZPG case also provides a useful baseline for comparison to other cases.

Many flows of interest differ from the canonical case. The surfaces of ships, aircraft, lifting and planning surfaces and turbomachinery components, for example, may be approximately smooth or flat in some locations, but in general, their boundary layers are subject to roughness and curvature effects. Curvature is often the cause of non-zero pressure gradients. Both favourable (FPG) and adverse (APG) pressure gradients are of fundamental and practical interest. Favourable pressure gradients stabilize the boundary layer, reduce turbulence, and if sufficiently strong can lead to relaminarization. Adverse pressure gradients are destabilizing and can lead to boundary layer separation.

Although not as extensive as in the ZPG case, considerable work has been done in non-ZPG boundary layers. Fundamental experimental studies include Aubertine & Eaton (2005), who considered a mild APG and noted differences in turbulence statistics from the ZPG case. Skåre & Krogstad (1994) considered a strong APG case near separation. Castillo & George (2001) considered both favourable and adverse pressure gradients and compared the results of several earlier studies. Jones, Marusic & Perry (2001) documented FPG sink flow cases. Harun *et al.* (2013) considered both FPG and APG effects. Computations have included the sink flow DNS of Spalart (1986) and the APG DNS of Kitsios *et al.* (2017). Skote, Henningson & Henkes (1998) considered self-similar APG cases. Lee & Sung (2009) and Lee (2017) considered equilibrium APG boundary layers with pressure gradients of various strength. Bobke *et al.* (2017) showed the history effects on APG boundary layers near equilibrium. These are just a few examples. Many more studies have documented boundary layers on airfoils for various applications.

While much has been learned from the studies in the literature, there is still limited documentation of the flow structure beyond the turbulence statistics, and limited information about the non-equilibrium development in boundary layers responding to changes in pressure gradients. Presumably, the types of structures documented in ZPG boundary layers by studies such as Adrian, Meinhart & Tomkins (2000) are still present in non-ZPG cases. The DNS studies of Lee & Sung (2009) and Lee (2017) have shown this for equilibrium APG flows, but such documentation is limited. The non-equilibrium response of the size and shape of these structures to changes in pressure gradient remains to be documented. The present study addresses these issues by considering fully turbulent boundary layers on smooth, flat walls subject to non-zero pressure gradients. Cases with a range of Reynolds numbers and mild to strong pressure gradients are presented. The magnitudes of the strongest pressure gradients approach, but remain below those necessary to cause relaminarization or separation. The present paper begins with an examination of how the mean velocity and turbulence statistics, along with the integral quantities and wall shear determined
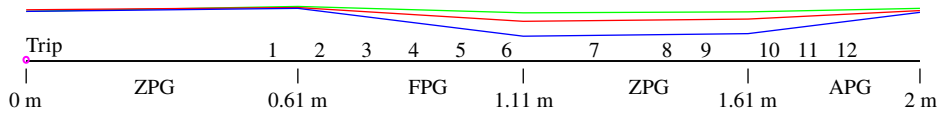
FIGURE 1. Cross-section of test section in streamwise–wall-normal plane. Three positions of upper wall shown: blue, ramp 1; red, ramp 2; green, ramp 3. Numbers in test section indicate streamwise measurement stations.

from them, change in response to the pressure gradient. This is followed by spatial correlations of the turbulence, which illustrate how turbulence structures respond to changes in the pressure gradient.

2. Experiments

Experiments were conducted in the water tunnel described by Volino, Schultz & Flack (2007). The test section was 2 m long, 0.2 m wide and nominally 0.1 m tall at the inlet of the test section. The lower wall was a flat plate that served as the test wall and included a trip near the leading edge, as shown in figure 1. The upper wall was comprised of four flat plates that were independently adjusted to set the pressure gradient. The upper wall and sidewalls provided optical access.

Flow was supplied to the test section from a 4000 l cylindrical tank. Water was drawn from the tank to two variable speed pumps operating in parallel and then sent to a flow conditioning section consisting of a diffuser containing perforated plates, a honeycomb, three screens and a three dimensional contraction. The test section followed the contraction. The free-stream turbulence level was 0.3 %. Water exited the test section through a perforated plate emptying into the cylindrical tank. The test fluid was filtered and deaerated water. A chiller was used to keep the water temperature constant to within 0.5 °C during all tests.

Boundary layer velocity measurements were obtained with a TSI FSA3500 two-component laser Doppler velocimeter (LDV). A four beam fibre optic probe was used to collect data in backscatter mode. The beams entered the test section through one of the sidewalls. A custom designed beam displacer was added to the probe to shift one of the four beams, resulting in three co-planar beams that were aligned parallel to the test wall. Additionally, a 2.6 : 1 beam expander was located at the exit of the probe to reduce the size of the measurement volume. The resulting probe volume diameter (d) was 45 µm with a probe volume length (l) of 340 µm. The corresponding measurement volume diameter and length in viscous length scales were $d^+ \leqslant 4.8$ and $l^+ \leqslant 36$. The flow was seeded with 2 µm diameter silver coated glass spheres. The data were collected in coincidence mode. For each velocity profile, the LDV probe was traversed to 46 locations within the boundary layer using a Velmex three-axis traverse with resolution of ± 5 µm in all directions. Data were typically acquired at each location in the boundary layer for 180–240 s, depending on the free-stream velocity, or until 50 000 random velocity samples were obtained.

The uncertainty in the mean streamwise velocity was 0.5 % of the free-stream velocity. The 95 % confidence interval uncertainty in the turbulence quantities was determined using the bootstrapping method and ranged from 2 % to 5 % in the Reynolds stresses. Uncertainties in triple products ranged from 10 % to 30 % depending on the quantity and the location in the boundary layer. More details of the uncertainty estimates are available in Volino (2020).

The wall friction velocity, u_τ, and skin friction coefficient, $C_f/2 = (u_\tau/U_\infty)^2$, were determined for each velocity profile using the method described in Volino & Schultz (2018) with an uncertainty in u_τ of 3 %. The method is based on the streamwise momentum equation and utilizes the measured mean streamwise velocity and Reynolds shear stress profiles. The Clauser chart method, which is based on fitting the mean profile to the law of the wall, is not applicable in all of the present cases because the strong pressure gradients cause deviation from the standard log law. In ZPG regions, u_τ from the present method and the Clauser chart method agreed to within 2 %.

Velocity field measurements were made using planar particle image velocimetry (PIV) at the same streamwise locations as the LDV profiles. At each location a streamwise–wall-normal (x–y) plane was acquired at the spanwise centreline of the test section, and streamwise–spanwise (x–z) planes were acquired at $y/\delta = 0.15$ and 0.4, where δ is the 99 % boundary layer thickness. The flow was seeded with the same particles used in the LDV measurements. For each plane, 1000 image pairs were acquired using a CCD camera with a 3320×2496 pixel array. Velocity vectors were obtained with TSI Insight 4G software using 32 pixel square windows with 50 % overlap. The field of view was 39 mm $\times$ 29 mm in the x–y plane, and 48 mm $\times$ 41 mm in the x–z plane.

2.1. *Test cases*

All test cases included a 0.6 m long ZPG development region at the inlet of the test section. The first measurement station was near the end of this section, and as shown in Volino (2020), the turbulent boundary layer was fully developed at this location, and both the mean flow and turbulence quantities agreed with the ZPG DNS results of Jiménez *et al.* (2010) at the corresponding Reynolds number. The top wall of the test section was slightly diverging in this region to account for the growth of the boundary layer.

The following section was set for a FPG from $x = 0.6$ m to 1.1 m, where x is the streamwise distance downstream of the trip. The FPG had a constant acceleration parameter,

$$K = \frac{\nu}{U_\infty^2} \frac{dU_\infty}{dx}, \tag{2.1}$$

where ν is the kinematic viscosity and U_∞ is the local free-stream velocity. A constant K FPG is a sink flow, which will reach equilibrium in all dimensionless quantities if given sufficiently long to develop.

The FPG region was followed by a ZPG recovery region extending from $x = 1.1$ m to 1.6 m. This was followed by a constant K APG region. The K value in the APG was set to half the magnitude of the upstream FPG in each case. A free-stream core was maintained between the test wall and upper wall boundary layers at all measurement locations. Downstream of the last station, the rapid growth of the boundary layers in the APG region eventually caused them to merge. Full equilibrium can only be achieved in FPG sink flows, but as explained in Bobke *et al.* (2017) based on the work of Mellor & Gibson (1966), near equilibrium, in which the mean velocity is streamwise invariant in defect coordinates, is possible in some cases when the free-stream velocity is described by $U_\infty = C(x - x_o)^m$, with C, x_o, and m constants. Near equilibrium can be achieved in the ZPG case ($m = 0$) and in APG cases when $m > -1/3$. In these cases, the pressure gradient parameter,

$$\beta = \frac{\delta^*}{\tau_o} \frac{dP}{dx} = Re_{\delta^*} \frac{-K}{C_f/2}, \tag{2.2}$$

(where δ^* is the displacement thickness, τ_o is the wall shear stress and P is pressure) will reach a constant in equilibrium. For constant K, $m = -1$, so the present APG flows do not approach or achieve equilibrium, and β continuously increases in the APG region, similar to the cases considered by Monty, Harun & Marusic (2011).

Three positions of the upper wall were used, as shown in figure 1. Three different inlet velocities, $U_{\infty o} = 0.5$, 1 and 2 m s^{-1}, were used, resulting in 8 experimental cases with K values shown in table 1. The cases with the same K value allow some separation of Reynolds number and acceleration effects. In the FPG, cases with the same K will eventually reach the same equilibrium condition if given long enough to develop, but those with a more aggressive setting of the upper wall will approach the sink flow condition more quickly. The momentum thickness Reynolds number, Re_θ, dropped with streamwise distance through the FPG region with the aggressive setting of the upper wall (ramp 1), remained nearly constant with the moderate setting (ramp 2) and rose (albeit more slowly than with a ZPG) in the cases with the mild setting (ramp 3). This Re_θ behaviour illustrates an unavoidable history dependence on the initial boundary layer thickness and Re_θ at the start of the FPG.

The twelve streamwise stations used for measurements are shown in table 2 and figure 1. Station 1 was near the end of the ZPG entry region, stations 2–6 were in the FPG region, stations 7–9 spanned the ZPG recovery and stations 10–12 were in the APG region. Table 1 gives boundary layer parameters for all cases including the friction Reynolds number, $Re_\tau = u_\tau \delta / \nu$; and the shape factor, H. The wake strength, Π, is defined as the difference between the measured velocity in wall coordinates at δ and the log law

$$\Pi = \frac{\kappa}{2} \left(0.99 U^+ - \left(\frac{1}{\kappa} \ln \delta^+ + B \right) \right), \quad (2.3)$$

where $\kappa = 0.384$. The value of the intercept, B, is set to best fit the data of each profile. For the ZPG region, B was close to the canonical ZPG value of 4.2 corresponding to $\kappa = 0.384$, as given by Nagib, Chauhan & Monkewitz (2007). In strong FPG regions, B was slightly higher, as will be shown below. For the APG, Monty *et al.* (2011) note that several studies with strong pressure gradients have shown a drop in B below the canonical value, but the difference is typically not as strong as in the FPG, and was small for the present cases. For cases with mild APGs ($\beta < 2.3$), Aubertine & Eaton (2005) reported agreement with the standard log law.

For comparison to the cases described above, data were also acquired for cases over the same Reynolds number range with a ZPG along the entire test section. These cases are presented in Volino (2020).

3. Results

3.1. *Mean velocity profiles*

The format for presentation of the results will be to show profiles of the various quantities for one of the stronger pressure gradient cases (case 2 in table 1) to illustrate how the boundary layer changes in response to the pressure gradient, and then to quantify and compare these changes in the streamwise direction for all cases. All cases had qualitatively similar behaviour, but as expected, there was considerable difference in the magnitude of the changes depending on the pressure gradient.

The mean streamwise velocity, U, is shown in figure 2. Figure 2(*a*) shows the profiles at St. 1–6 in outer, defect coordinates. Also shown is a comparison

St.	U_∞ (m s⁻¹)	u_τ (m s⁻¹)	δ (mm)	Re_θ	$Re_\tau = \delta^+$	$H = \delta^*/\theta$	β	Π
	Case 1: Ramp 1, $K_{FPG} = 2 \times 10^{-6}$, $U_{\infty o} = 0.5$ m s⁻¹, Symbol = ●							
1	0.490	0.0239	12.89	721	304	1.506	−0.91	0.238
2	0.535	0.0266	11.52	668	303	1.517	−0.82	0.163
3	0.573	0.0281	12.54	669	360	1.418	−0.79	−0.129
4	0.644	0.0320	11.34	626	356	1.428	−0.72	−0.175
5	0.722	0.0350	10.95	611	394	1.415	−0.74	−0.324
6	0.967	0.0475	9.17	607	448	1.424	−0.72	−0.370
7	0.978	0.0440	10.28	981	466	1.437	0	0.128
8	0.971	0.0435	12.45	1381	559	1.434	0	0.284
9	0.960	0.0404	15.69	1855	647	1.442	0	0.465
10	0.904	0.0340	18.39	2294	644	1.520	2.47	0.920
11	0.851	0.0290	21.66	2765	641	1.612	3.84	1.444
12	0.810	0.0248	25.73	3291	651	1.701	5.97	2.084
	Case 3: Ramp 2, $K_{FPG} = 1 \times 10^{-6}$, $U_{\infty o} = 0.5$ m s⁻¹, Symbol = □							
1	0.490	0.0233	15.03	877	347	1.480	−0.57	0.273
2	0.507	0.0241	16.31	950	389	1.448	−0.61	0.195
3	0.533	0.0259	16.36	932	419	1.425	−0.56	0.064
4	0.556	0.0270	16.58	943	443	1.405	−0.56	−0.026
5	0.588	0.0285	16.39	952	462	1.391	−0.56	−0.082
6	0.635	0.0310	16.49	935	506	1.371	−0.54	−0.161
7	0.649	0.0307	18.81	1207	571	1.401	0	0.047
8	0.650	0.0291	20.84	1486	600	1.429	0	0.252
9	0.650	0.0286	22.13	1641	626	1.428	0	0.287
10	0.639	0.0269	24.28	1867	646	1.449	0.76	0.470
11	0.626	0.0252	27.23	2094	679	1.474	0.95	0.649
12	0.613	0.0239	27.55	2215	651	1.497	1.09	0.806

U_∞ (m s⁻¹)	u_τ (m s⁻¹)	δ (mm)	Re_θ	$Re_\tau = \delta^+$	$H = \delta^*/\theta$	β	Π
Case 2: Ramp 1, $K_{FPG} = 1 \times 10^{-6}$, $U_{\infty o} = 1$ m s⁻¹, Symbol = ■							
0.980	0.0433	14.30	1583	592	1.423	−1.15	0.323
1.053	0.0463	14.18	1623	654	1.366	−1.15	0.106
1.167	0.0530	13.68	1522	719	1.323	−0.98	−0.097
1.284	0.0595	13.01	1470	771	1.308	−0.89	−0.190
1.470	0.0675	12.00	1363	807	1.302	−0.84	−0.298
1.823	0.0850	9.10	1133	773	1.330	−0.69	−0.351
2.006	0.0866	10.91	1948	944	1.385	0	0.115
1.979	0.0805	12.25	2665	985	1.412	0	0.448
1.977	0.0779	14.46	3285	1125	1.408	0	0.526
1.836	0.0639	17.64	4288	1126	1.499	2.65	1.121
1.730	0.0547	20.71	5186	1132	1.576	4.09	1.674
1.649	0.0465	24.59	6255	1132	1.678	6.60	2.362
Case 4: Ramp 2, $K_{FPG} = 0.5 \times 10^{-6}$, $U_{\infty o} = 1$ m s⁻¹, Symbol = ▽							
0.978	0.0430	13.39	1578	570	1.427	−0.58	0.345
1.014	0.0444	14.91	1768	655	1.399	−0.65	0.278
1.065	0.0460	15.10	1763	687	1.370	−0.65	0.171
1.112	0.0490	15.03	1742	729	1.352	−0.61	0.070
1.177	0.0520	15.22	1763	783	1.337	−0.60	0.018
1.273	0.0562	14.20	1685	789	1.334	−0.58	−0.021
1.303	0.0550	16.09	2156	875	1.376	0	0.221
1.301	0.0535	18.82	2680	996	1.390	0	0.339
1.297	0.0524	20.28	3000	1052	1.388	0	0.422
1.275	0.0497	22.09	3396	1086	1.410	0.79	0.569
1.247	0.0468	22.56	3607	1045	1.442	0.92	0.781
1.218	0.0450	24.08	3846	1072	1.454	1.02	0.860

TABLE 1. For caption see next page.

Case 6: Ramp 3, $K_{FPG}=0.5\times10^{-6}$, $U_{\infty o}=0.5$ m s^{-1}, Symbol = ▽ and **Case 8: Ramp 3, $K_{FPG}=0.125\times10^{-6}$, $U_{\infty o}=2$ m s^{-1}, Symbol = ◁**

St.	U_∞ (m s^{-1})	u_τ (m s^{-1})	δ (mm)	Re_θ	$Re_\tau=\delta^+$	$H=\delta^*/\theta$	β	Π	U_∞ (m s^{-1})	u_τ (m s^{-1})	δ (mm)	Re_θ	$Re_\tau=\delta^+$	$H=\delta^*/\theta$	β	Π
1	0.491	0.0231	11.40	673	260	1.578	−0.24	0.450	1.962	0.0796	11.83	2765	931	1.407	−0.30	0.478
2	0.501	0.0243	12.72	744	306	1.498	−0.24	0.248	2.000	0.0820	12.90	3014	1047	1.381	−0.31	0.368
3	0.513	0.0245	15.08	852	366	1.459	−0.27	0.149	2.049	0.0847	13.48	3131	1129	1.365	−0.31	0.292
4	0.522	0.0250	15.73	876	389	1.451	−0.28	0.120	2.081	0.0861	14.09	3270	1201	1.356	−0.32	0.250
5	0.535	0.0255	16.25	933	410	1.435	−0.29	0.117	2.131	0.0884	14.56	3373	1273	1.346	−0.33	0.214
6	0.552	0.0262	17.46	1014	453	1.418	−0.32	0.083	2.199	0.0909	15.32	3602	1378	1.337	−0.35	0.193
7	0.560	0.0256	21.05	1272	533	1.418	0	0.196	2.231	0.0890	17.22	4212	1517	1.350	0	0.312
8	0.559	0.0248	23.54	1497	578	1.431	0	0.306	2.235	0.0868	19.09	4831	1640	1.358	0	0.392
9	0.559	0.0241	25.86	1690	646	1.437	0	0.398	2.233	0.0852	20.60	5336	1737	1.367	0	0.461
10	0.553	0.0234	28.02	1884	649	1.440	0.38	0.460	2.210	0.0828	22.28	5800	1825	1.374	0.36	0.531
11	0.548	0.0227	29.64	2000	666	1.450	0.42	0.546	2.192	0.0806	23.22	6083	1852	1.381	0.39	0.605
12	0.544	0.0222	31.23	2122	686	1.456	0.46	0.600	2.173	0.0790	24.32	6386	1901	1.387	0.42	0.665

Case 5: Ramp 2, $K_{FPG}=0.25\times10^{-6}$, $U_{\infty o}=2$ m s^{-1}, Symbol = ◇ and **Case 7: Ramp 3, $K_{FPG}=0.25\times10^{-6}$, $U_{\infty o}=1$ m s^{-1}, Symbol = ◈**

St.	U_∞ (m s^{-1})	u_τ (m s^{-1})	δ (mm)	Re_θ	$Re_\tau=\delta^+$	$H=\delta^*/\theta$	β	Π	U_∞ (m s^{-1})	u_τ (m s^{-1})	δ (mm)	Re_θ	$Re_\tau=\delta^+$	$H=\delta^*/\theta$	β	Π
1	1.956	0.0782	12.35	2947	955	1.413	−0.65	0.508	0.985	0.0435	13.33	1541	574	1.428	−0.28	0.318
2	2.035	0.0836	13.07	3094	1081	1.371	−0.63	0.340	1.003	0.0430	14.63	1687	622	1.403	−0.32	0.296
3	2.134	0.0895	12.78	2994	1133	1.343	−0.57	0.169	1.030	0.0440	14.85	1700	647	1.390	−0.32	0.220
4	2.229	0.0950	13.13	2973	1234	1.322	−0.54	0.050	1.051	0.0450	15.81	1807	704	1.376	−0.34	0.180
5	2.367	0.1010	13.13	3007	1312	1.307	−0.54	0.008	1.081	0.0465	16.22	1847	746	1.365	−0.34	0.132
6	2.554	0.1090	12.77	3029	1377	1.299	−0.54	−0.034	1.116	0.0483	17.05	1987	815	1.358	−0.36	0.134
7	2.617	0.1060	15.10	3906	1583	1.334	0	0.223	1.126	0.0470	19.97	2427	929	1.371	0	0.268
8	2.615	0.1018	17.73	4837	1796	1.352	0	0.343	1.124	0.0461	22.40	2885	1022	1.390	0	0.402
9	2.606	0.1000	17.93	5240	1774	1.362	0	0.429	1.124	0.0451	23.98	2187	1070	1.398	0	0.451
10	2.553	0.0937	19.77	6012	1833	1.388	0.77	0.633	1.112	0.0440	25.23	3371	1098	1.399	0.38	0.502
11	2.493	0.0882	21.27	6556	1856	1.410	0.92	0.801	1.102	0.0426	27.07	3671	1141	1.412	0.43	0.605
12	2.433	0.0827	22.92	7142	1875	1.439	1.11	1.003	1.091	0.0413	28.63	3891	1170	1.423	0.48	0.675

TABLE 1 (cntd). Experimental conditions.

St.	1	2	3	4	5	6	7	8	9	10	11	12
x (m)	0.590	0.681	0.772	0.845	0.938	1.105	1.272	1.439	1.607	1.673	1.740	1.806
Case 1	○	▽	□	△	◇	◁	∗	▷	+	★	×	✩
x (m)	0.560	0.681	0.772	0.845	0.938	1.060	1.272	1.439	1.555	1.673	1.740	1.806
Cases 2–8												

TABLE 2. Measurement station streamwise locations.
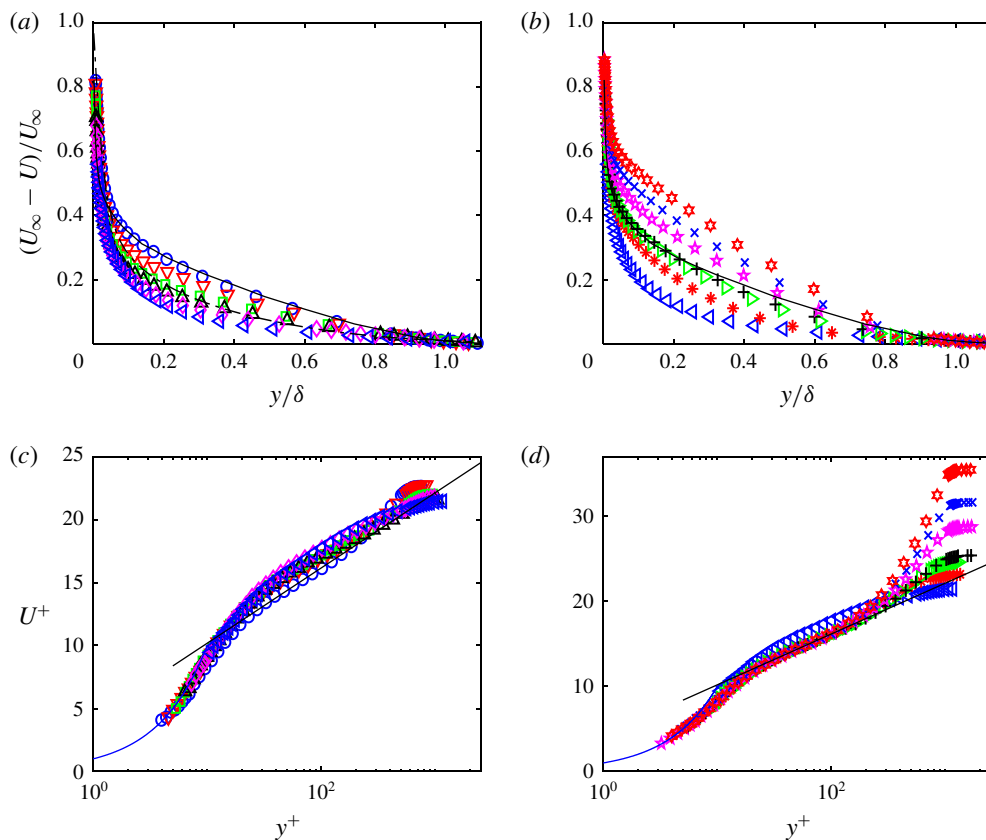
FIGURE 2. Mean streamwise velocity profiles for case 2, (*a*) defect coordinates for St. 1–6, (*b*) defect coordinates for St. 6–12, (*c*) inner scaling for St. 1–6, (*d*) inner scaling for St. 6–12. Symbols from table 2. Lines in (*a,b*): —— canonical ZPG comparison, — · — Spalart (1986) equilibrium sink flow DNS. Lines in (*c,d*): —— (blue) $U^+ = y^+$, —— (black) log law with $\kappa = 0.384$, $B = 4.2$.

profile from the canonical ZPG study of Volino (2020) taken at $Re_\theta = 6340$, and an equilibrium sink flow profile from Spalart (1986). The ZPG study showed essentially no variation in these coordinates for $y/\delta > 0.2$ over the full range of Re_θ considered. The St. 1 profile, at the end of the initial ZPG entrance region, agrees with the ZPG comparison profile. The profiles at the subsequent stations drop in response to the FPG, and by St. 5 are below the equilibrium result, which will be discussed below.
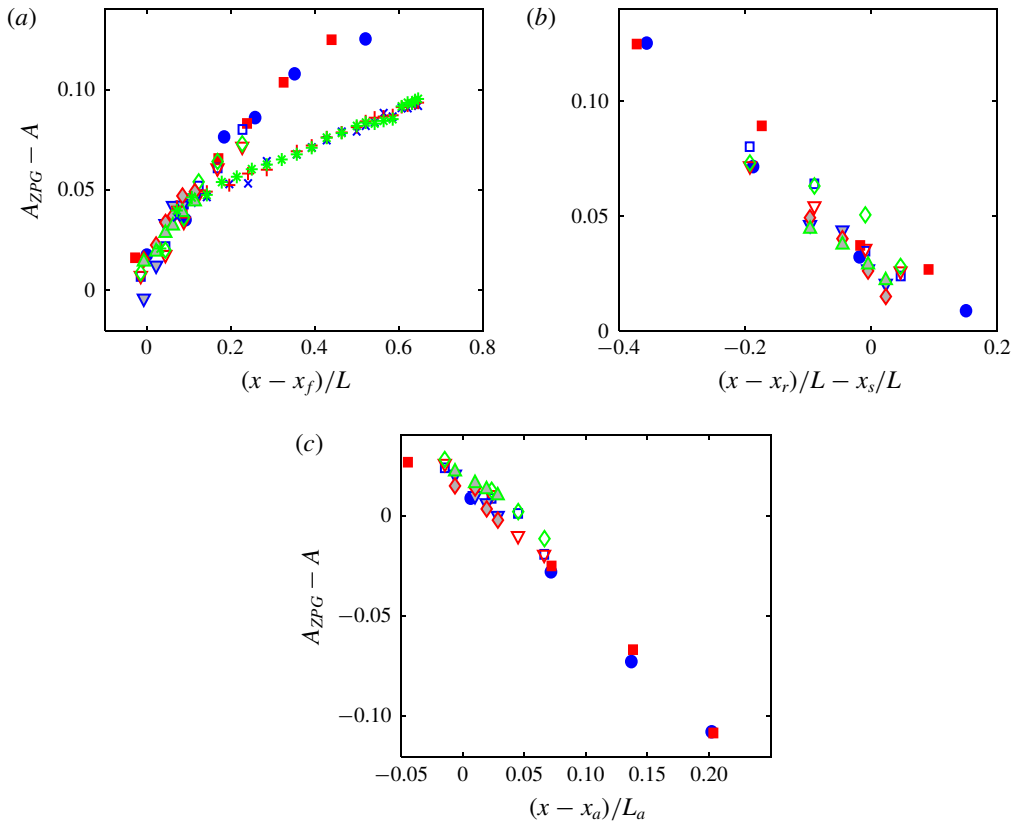
FIGURE 3. Difference in $A = (U_\infty - U)/U_\infty$ between ZPG and non-ZPG mean velocity defect profiles at $y/\delta = 0.4$. ZPG and non-ZPG compared at same Re_θ. (*a*) FPG St. 1–6, (*b*) ZPG St. 6–9, (*c*) APG St. 9–12. Symbols from table 1 for cases of present study. Symbols for Jones (1998) results: $\times$, $K = 0.539 \times 10^{-6}$; $+$, $K = 0.359 \times 10^{-6}$; $*$, $K = 0.270 \times 10^{-6}$.

The profiles in the recovery and APG regions are shown in figure 2(*b*), with the St. 6 profile and the ZPG comparison profile from figure 2(*a*) repeated for reference. The profiles rise through the recovery region and reach agreement with the ZPG comparison case by St. 9. In the APG, there is a continuous increase above the ZPG profile.

To quantify the variation from ZPG conditions for all cases, figure 3 shows the difference between the measured defect velocity and the corresponding velocity in a ZPG profile from Volino (2020). The difference is taken at a representative location of $y/\delta = 0.4$, and is shown as a function of streamwise location. The location $y/\delta = 0.4$ was selected as about the centre of the region where the change in the profile was most pronounced. Essentially equivalent results were produced when alternate locations such as $y/\delta = 0.3$ or 0.5 were selected. An integrated change over a range in y was also tried, and this also gave similar results, but produced more scatter, presumably because it included locations where the change was small. For the FPG region in figure 3(*a*), the streamwise coordinate is normalized as $(x - x_f)/L$, where x_f is the location at the start of the FPG, and $L = \nu/(K_{FPG}U_{\infty f})$ is the FPG sink flow length, with $U_{\infty f}$ the free-stream velocity at the start of the FPG. This normalization

was chosen because the profiles must reach equilibrium by the end of the sink flow length. The data for all cases collapse onto a single curve for the FPG region. The cases with the more aggressive ramps proceed farther along the curve, but none has clearly plateaued to an equilibrium by the end of the FPG region. It is interesting that all cases appear to proceed along the same curve, regardless of differences in the test section geometry, Reynolds number, K, or the pressure gradient parameter, β. Also shown are the sink flow experimental results of Jones *et al.* (2001), as tabulated in Jones (1998). In their cases, with three different inlet velocities and K ranging from 0.27×10^{-6} to 0.54×10^{-6}, the results also follow a single curve, but with a different slope than the present study. The difference may be due to differences in the inlet condition to the FPG. In the present study, all cases had equal length ZPG development regions after the trip, and achieved fully developed turbulent ZPG boundary layer conditions. In the Jones *et al.* (2001) study, the FPG began at the start of the test section, immediately after the trip.

The sink flow DNS of Spalart (1986), who considered K between 1.5×10^{-6} and 2.75×10^{-6}, showed that the equilibrium profile shape in defect coordinates exhibited very little variation with K for $y/\delta > 0.1$. This is consistent with the findings of Castillo & George (2001), who noted a common profile shape was reached for all FPG cases. At $y/\delta = 0.4$, the difference between the equilibrium sink flow and ZPG profiles, in the coordinates of figure 3, is about 0.09. This is close to the St. 6 results for cases 3–5 with ramp 2 and the most downstream results of Jones *et al.* (2001), suggesting that the boundary layer was close to reaching its equilibrium condition. The profiles in all of these cases matched each other and the equilibrium sink flow result, even with K as low as 0.25×10^{-6}. In the ramp 3 cases (6–8), the boundary layer was still in a non-equilibrium state with Re_θ continuing to rise, and the defect profiles remained above the equilibrium profile, as shown by the $y/\delta = 0.4$ values in figure 3(*a*). With ramp 1 (cases 1 and 2), the boundary layer was again still not in equilibrium at St. 6, but with Re_θ dropping. This led to an overshoot of the equilibrium profile, as shown in figure 2. Presumably, if the FPG region of the test section were longer, the profile development would have eventually reversed, rising toward equilibrium. To explore this, two-dimensional, Reynolds averaged Navier–Stokes (RANS) calculations were done using the boundary layer code TEXSTAN (an extension of STAN5 by Crawford & Kays (1976)). The low Reynolds number, two-equation turbulence model of Chien (1982) was used for turbulence closure. The recommended settings were used for all constants; no attempt was made to optimize or tune the computations. Cases were run using the boundary conditions of the present study through the inlet and FPG regions, and for the Jones *et al.* (2001) cases. The streamwise length of the FPG region was extended farther in the computations than in the experiments. The computed mean velocity profiles did not match the experiments precisely, but did show the correct trends with pressure gradient. In defect coordinates, there was no difference between cases with the same geometry and different inlet velocities, in agreement with the experiments. As shown in table 1, at each station, β was the same for all cases with the same ramp. This suggests that it is the geometry and the resulting pressure gradient parameter, β, that are significant, not the Reynolds number or K. Results extracted from the calculations are shown in figure 4. Comparison with figure 3(*a*) shows good agreement with the exception that the calculation results are systematically low by 0.02 compared to the experiments. The variation with different geometries and upstream development are correctly predicted. The overshoot and predicted return to equilibrium is shown for the ramp 1 cases. The predictions suggest that all cases would eventually reach the same dimensionless profile by the end of the sink flow region.
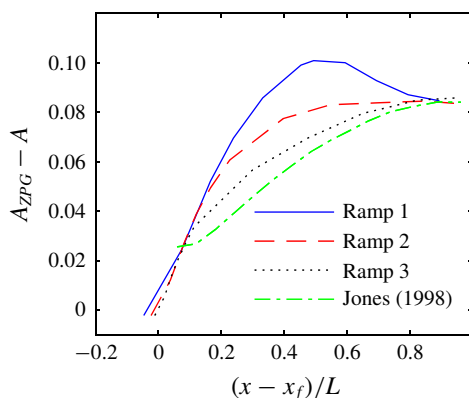
FIGURE 4. RANS prediction of difference in $A = (U_\infty - U)/U_\infty$ between ZPG and non-ZPG mean velocity defect profiles at $y/\delta = 0.4$ in FPG region.

The recovery region data are shown in figure 3(b). The streamwise coordinate is normalized as $(x - x_r)/L - x_s/L$, where x_r is the location at the start of the ZPG recovery, and $x_s = 0.7(x_r - x_f)$. The x_s term accounts for the cases with more aggressive ramps (lower L) having departed more from ZPG conditions, and therefore requiring a longer recovery distance to resume canonical ZPG behaviour. The constant 0.7 was determined empirically to collapse the data. Presumably it would decrease towards zero if the FPG region were longer, allowing all cases to more closely approach the sink flow equilibrium condition at the start of the recovery.

The APG region data are shown in figure 3(c). The streamwise distance is normalized as $(x - x_a)/L_a$, where x_a is the location at the start of the APG, and $L_a = \nu/(K_{APG}U_{\infty a})$, with $U_{\infty a}$ the free-stream velocity at the start of the FPG. Since the recovery to a canonical ZPG profile was essentially complete in all cases, all begin the APG under similar conditions, and the results for all cases collapse unto the same curve. The normalizing length, L_a, was chosen using the same definition as for the sink flow, and can be used in the present cases because K is constant. An alternative for the APG region is to use the local pressure gradient parameter, β. Figure 5(a) shows β as a function of $(x - x_a)/L_a$ for all cases. It increases monotonically with x, and all cases fall roughly onto the same curve, although closer inspection shows different slopes for the three ramps. This means that the results in figure 3(c) could be shown as a function of β, as shown in figure 5(b). The same is true for all of the APG results below. The ability to cast the present APG results as a function of the local pressure gradient parameter suggests a possible independence of upstream history. Monty *et al.* (2011) found similar collapse of profiles with different Reynolds numbers and streamwise locations when β was held constant, even for cases that were not in equilibrium. It is clear, however, that this result is not universal. Bobke *et al.* (2017) showed history effects. The present cases and those of Monty *et al.* (2011) started from a fully developed ZPG boundary layer and had monotonically increasing β. Perhaps the present results do not indicate a history independence, but behave similarly because they have the same β history in the scaling of figure 5(a). Note that the streamwise development cannot be shown as a function of β in the ZPG region (where $\beta = 0$) or in the FPG in the present cases where β does not change monotonically in the streamwise direction.

The mean profiles for case 2 are shown in inner coordinates in figures 2(c) and 2(d). The standard log law with $\kappa = 0.384$ and $B = 4.2$ is shown for reference. In the FPG,
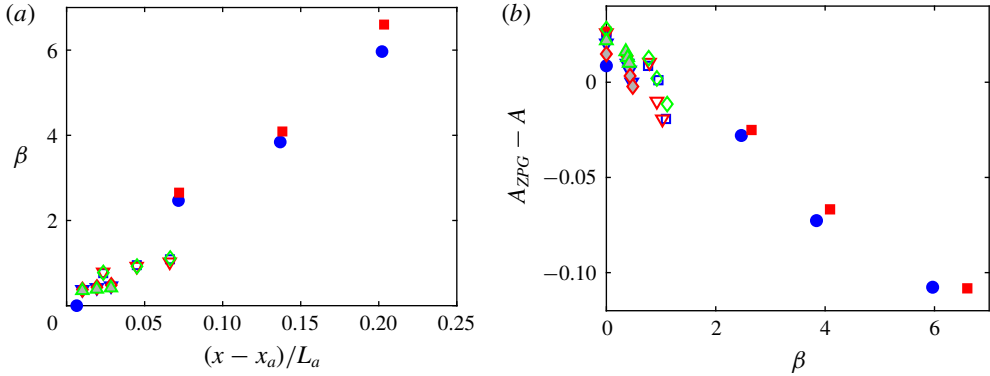
FIGURE 5. Development of APG region as function of local pressure gradient. (*a*) β as function of streamwise coordinate of figure 3(*c*), (*b*) *A* of figure 3(*c*) as function of β.

the profiles rise above the log law, and the wake is suppressed. The departure from the log law is slightly larger than predicted by the sink flow DNS of Spalart (1986). In the recovery, the profiles return to the log law, and the growth of the wake resumes. The profile matches the canonical ZPG boundary layer at the same Re_θ by St. 8. In the APG region, agreement with the log law continues, but growth of the wake becomes rapid. This growth of the wake can be quantified, and is shown in the Appendix to follow the streamwise scaling shown in figure 3.

Quantities obtained from the mean velocity profile are considered next. The boundary layer thickness provides one measure of the response to the pressure gradient. In the FPG region, strong acceleration with ramp 1 caused δ to drop slowly, and the momentum and displacement thicknesses to drop more rapidly. With ramp 2, δ remained nearly constant, while δ^* and θ dropped slowly after an initial rise. With the weaker acceleration of ramp 3, δ rose, δ^* remained constant and θ rose slowly. In the recovery region, all the boundary layer thicknesses resumed the growth rate expected for a ZPG boundary layer. In the APG, all the thicknesses grew more rapidly.

The skin friction coefficient is shown as a function of Re_θ in figure 6(*a*). Other quantities determined from the mean profile (Re_τ, H) are shown in the Appendix. For the FPG and recovery regions, C_f agrees with a typical ZPG textbook correlation, $C_f = 0.025 Re_\theta^{-0.25}$ taken from Kays & Crawford (1980). For an equilibrium sink flow, it can be shown that $C_f = 2K(1 + H)Re_\theta$. For the ramp 2 cases, the measured C_f agrees with the sink flow value by station 6, while for the ramp 1 cases the measured C_f is below the sink flow value and for the ramp 3 cases it is above the sink flow value. These results are consistent with the station 6 Re_θ values noted above, which are near their equilibrium value for the ramp 2 cases, but still dropping or rising toward equilibrium for the ramp 1 and 3 cases, respectively. This was also shown in figures 3(*a*) and 4, which indicate that a longer development length would be needed for the mean velocity profiles of the ramp 1 and 3 cases to reach equilibrium. In the APG region, C_f drops significantly below the ZPG correlation as β rises. In the limit of boundary layer separation, an APG drives the mean velocity gradient near the wall toward zero as the boundary layer thickness and Re_θ remain finite. The drop below the ZPG correlation should therefore be expected even for attached flows. It must be some function of the pressure gradient, and a simple relationship would be a linear function of β. Multiplying C_f by $(1 + \beta/10)$ results in agreement of all the cases, as shown in
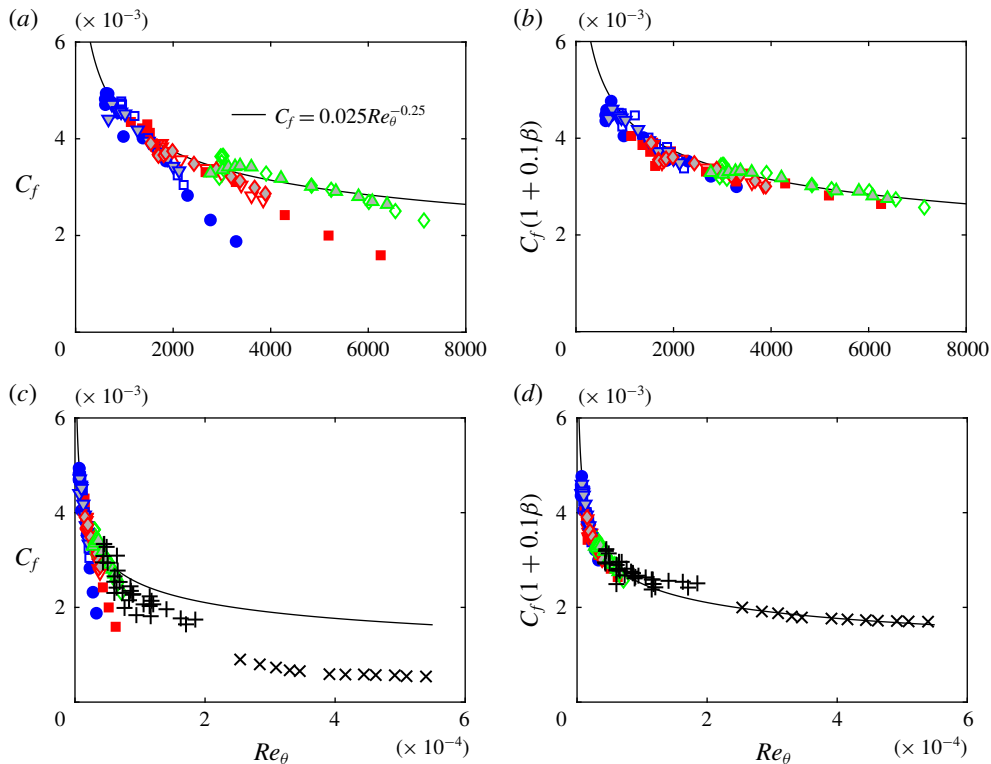
FIGURE 6. Skin friction coefficient, C_f. Symbols for present cases from table 1. (a) Present study, uncorrected; (b) present study with $(1 + \beta/10)$ correction; (c) uncorrected and including results of Harun *et al.* (2013) (+) and Skåre & Krogstad (1994) (×); (d) corrected with $(1 + \beta/10)$ and including Harun *et al.* (2013) and Skåre & Krogstad (1994) results.

figure 6(b). The results of Skåre & Krogstad (1994) and Harun *et al.* (2013) are added in figure 6(c,d). In agreement with the present cases, the APG causes the expected drop in C_f below the ZPG correlation, and the $(1 + \beta/10)$ correction re-establishes agreement. The same correction also agrees with the APG DNS results of Lee (2017) and the experiments of Monty *et al.* (2011). The linear form of the correction and the constant 10 were determined empirically, but the trend of the correction is expected, as explained above. It applies to the cases in figure 6, which are near equilibrium or have monotonically increasing β. It is not necessarily useful for arbitrary pressure gradients, and did not agree with data from cases with different pressure gradient histories, such as those presented in Bobke *et al.* (2017).

3.2. *Reynolds stresses*

The boundary layer turbulence is considered next. Figure 7 shows profiles of the streamwise component of the Reynolds normal stress, $\overline{u'^2}$, for case 2. In outer coordinates there is a drop in the outer layer in the FPG region, similar to that in the mean velocity profiles of figure 2(a). For the ramp 1 cases, the drop slightly overshoots the equilibrium sink flow result. The overshoot is not seen with the milder pressure gradients, again similar to the mean flow. By the end of the recovery region,
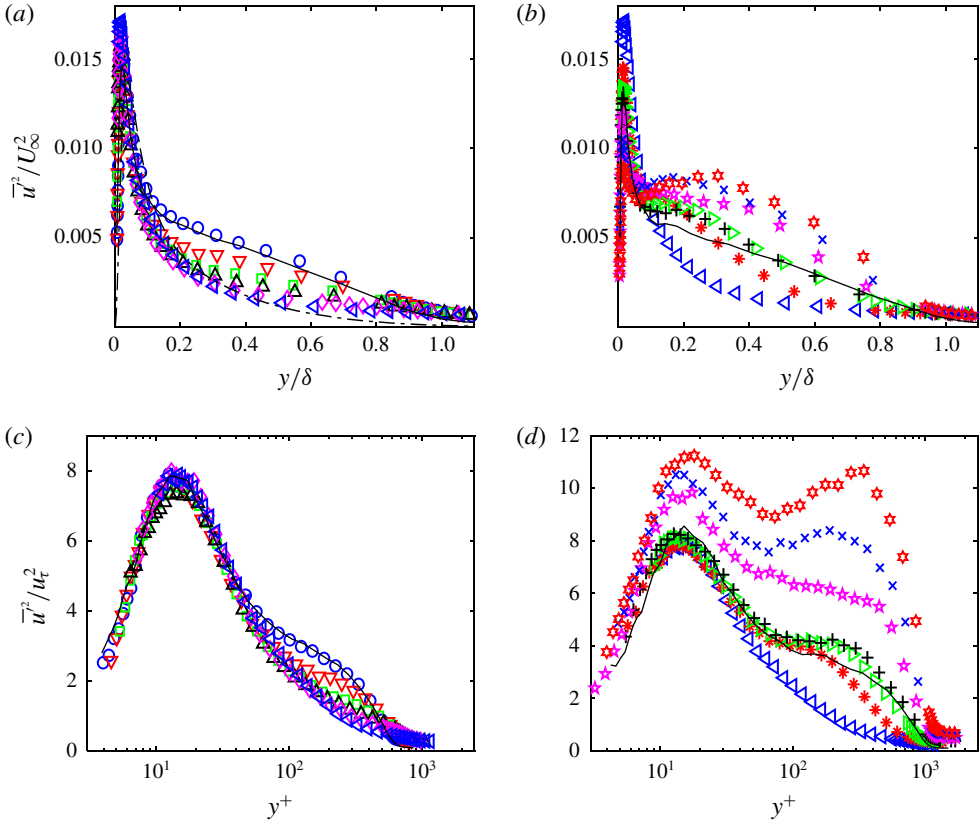
FIGURE 7. Streamwise Reynolds normal stress profiles for case 2, (*a*) outer coordinates for St. 1–6, (*b*) outer coordinates for St. 6–12, (*c*) inner coordinates for St. 1–6, (*d*) inner coordinates for St. 6–12. Symbols from table 2. Lines: —— canonical ZPG comparison, — · — Spalart (1986) equilibrium sink flow DNS.

there is good agreement with the canonical ZPG boundary layer. In the APG, the profiles rise above the ZPG result. The differences between the FPG results for all cases and the canonical ZPG case at the same Re_θ are shown in figure 8(*a*) in the format of figure 3. (As an alternative, the comparison could also be done at matching Re_τ in the ZPG case instead of Re_θ. This was done for all of the quantities of the present study with virtually no change in the results or conclusions.) As above, $y/\delta = 0.4$ is chosen as a representative location for the comparison. The results do not collapse. At a given K, the values rise more quickly at the lower Reynolds numbers. For $K = 1 \times 10^{-6}$, for example, case 3 reaches the same values as case 2 in about half the dimensionless streamwise distance. The mean streamwise velocity profile responds directly to the pressure gradient, as the pressure forces act on the mean momentum of the fluid. The turbulence quantities are then expected to respond to the changes in the mean velocity, and it is conjectured that the response occurs as a function of not only the sink flow length (along with the mean flow) but also the eddy turnover distance, which scales with the boundary layer thickness, δ. The normalizing length for the development of the $\overline{u'^2}$ profiles is, therefore, modified to $L^* = LRe_{\delta_f} = K/\delta_f$, where $Re_{\delta_f} = U_{\infty f}\delta_f/\nu$ and δ_f is the boundary layer thickness at the start of the FPG. This normalization is shown in figure 8(*b*), and although
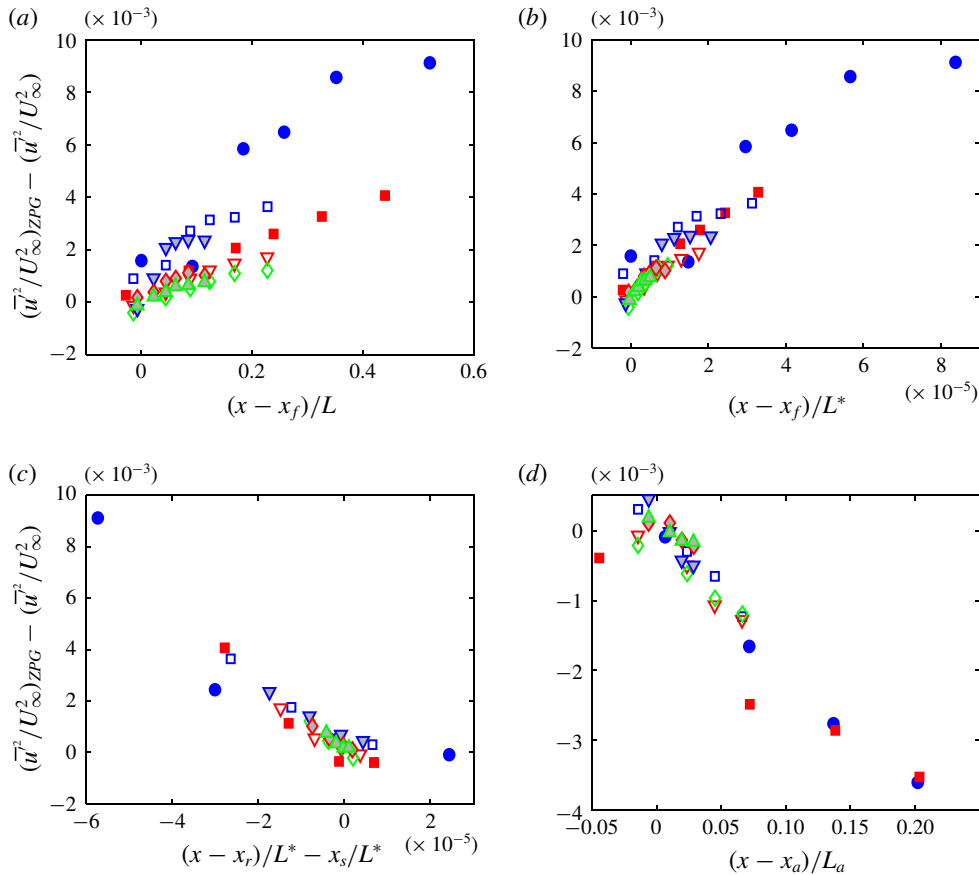
FIGURE 8. Difference between ZPG and non-ZPG $\overline{u'^2}/U_\infty^2$ profiles at $y/\delta = 0.4$. ZPG and non-ZPG compared at same Re_θ. (*a*) FPG St. 1–6, (*b*) FPG St. 1–6, (*c*) ZPG St. 6–9, (*d*) APG St. 9–12. Symbols from table 1.

determined empirically, appears to work well. It will also be seen to work well with all of the turbulence quantities of the present study. For the data of Jones (1998), an appropriate Re_{δ_f} for streamwise scaling was not as clear, since the FPG was not preceded by a ZPG region. His results did show, however, that the difference between the FPG and canonical ZPG profiles approached an equilibrium that roughly matched the most downstream results of the present study for cases with the same K. The present results show that the most downstream magnitude of each case in figure 8(*b*) increases with K. For K between 0.27×10^{-6} and 0.539×10^{-6}, the results of Jones (1998) reached an equilibrium magnitude of about 0.002, which is roughly consistent with the present cases. If the recovery region is considered a reverse of the FPG, the same streamwise scaling of the streamwise distance might apply there as well, as shown in figure 8(*c*). In the APG region, shown in figure 8(*d*), the same scaling is used as for the mean velocity in figure 3(*c*). This indicates that the $\overline{u'^2}$ response to the APG does not exhibit the same Reynolds number dependence that it does in the FPG and recovery. As will be further shown below, when the outer flow is strained by a FPG, there is a drop in the dimensional magnitude of the turbulence quantities.
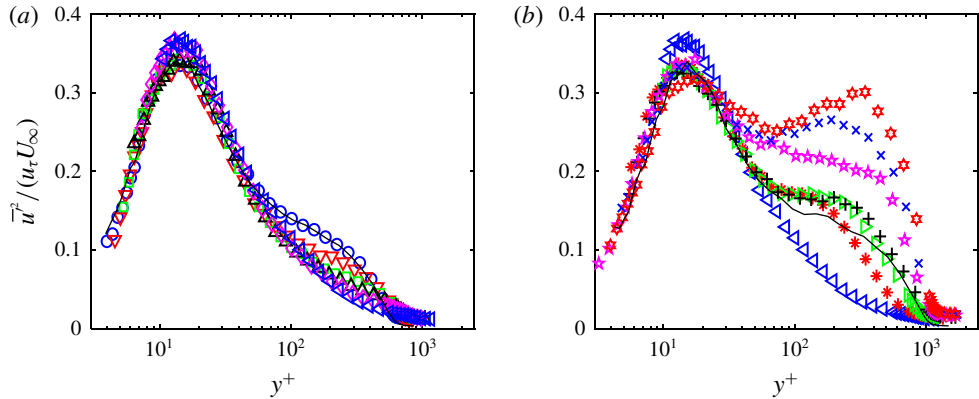
FIGURE 9. Streamwise Reynolds normal stress profiles for case 2 with mixed scaling, (*a*) St. 1–6, (*b*) St. 6–12. Symbols from table 2. Lines: —— canonical ZPG comparison.

In an APG the initial response is different, with the magnitude of the turbulence quantities remaining approximately frozen while the mean velocity drops.

The $\overline{u'^2}$ results are shown in inner coordinates in figure 7(*c*,*d*). In the FPG and recovery regions there is little change of the inner peak. The inner peak is due primarily to fluctuations across the high mean shear near the wall (i.e. inactive motions as explained by Bradshaw (1967)), so the peak scales with the wall shear. In the APG, the rapid drop in the wall shear relative to the turbulence already present in the boundary layer causes the inner peak to rise. Lee & Sung (2009) found using quadrant analysis that sweep motions from the outer part of the boundary layer have more influence on the inner region of APG flows, and the rise of the inner peak in response to the rise of the outer peak is consistent with this. It will be discussed further with the quadrant analysis results below. In all regions, the location of the inner peak remains fixed at $y^+ = 15$, consistent with experimental and DNS results in the literature and the dependence on the near-wall mean shear. Farther from the wall, $\overline{u'^2}$ is suppressed in the FPG and appears to collapse toward an equilibrium. The recovery to ZPG conditions is rapid, and there is a large rise of the outer peak in the APG. The streamwise development of the $\overline{u'^2}/u_\tau^2$ profiles was essentially the same as shown in figure 8 for the $\overline{u'^2}/U_\infty^2$ profiles. That is, the same scaling of the streamwise distance applied for both the inner and outer scaled $\overline{u'^2}$. The same was also true for the other turbulence quantities shown below.

The case 2 $\overline{u'^2}$ profiles are shown again in figure 9 using the mixed scaling of DeGraaff & Eaton (2000). In these coordinates there is a small rise in the inner peak in the FPG region, but much better collapse in the APG. For the APG, this supports the idea that the inner peak depends on both the local mean shear, which scales with u_τ, and the increased influence of the outer region, which scales with U_∞. The trends farther from the wall are the same as with standard inner scaling.

The $\overline{v'^2}$ profiles for all cases have the same behaviour as the Reynolds shear stress, and the same conclusions and scaling apply to $\overline{v'^2}$ and $-\overline{u'v'}$. The $-\overline{u'v'}$ are considered next, with an example of the $\overline{v'^2}$ profiles presented for comparison in the Appendix. The case 2 profiles are shown in figure 10. The inner peak observed in $\overline{u'^2}$ is not present in $-\overline{u'v'}$, but for the rest of the profile the trends with the pressure gradient in
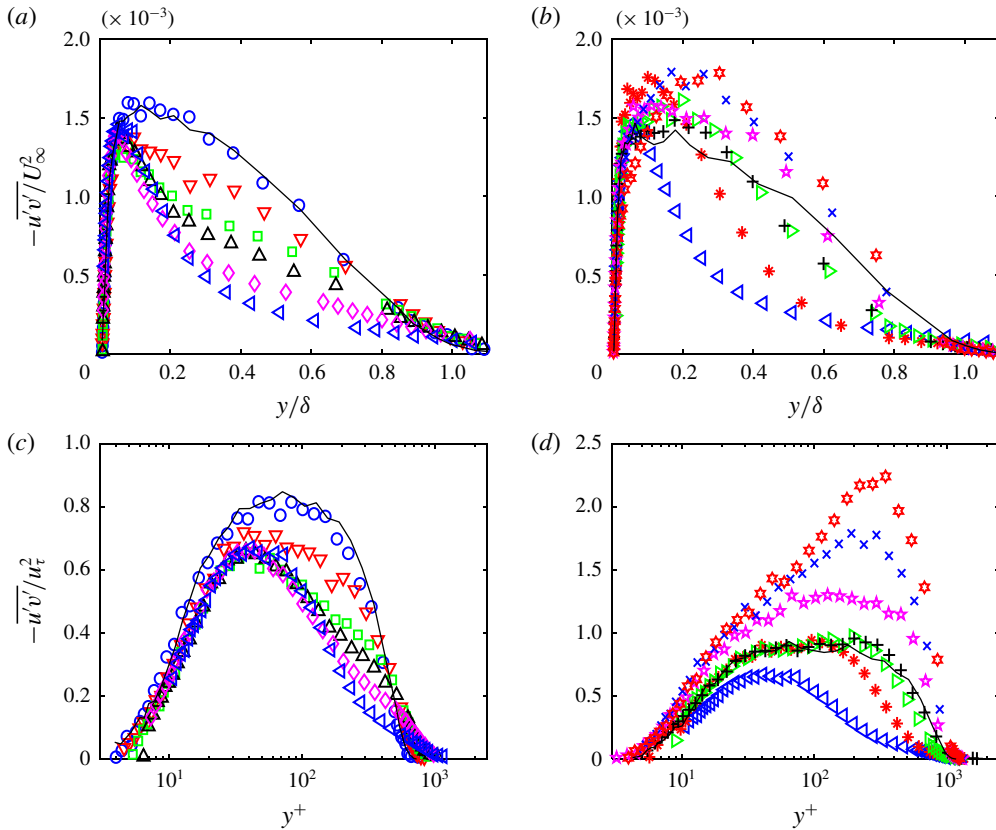
FIGURE 10. Reynolds shear stress profiles for case 2, (*a*) outer scaling for St. 1–6, (*b*) outer scaling for St. 6–12, (*c*) inner scaling for St. 1–6, (*d*) inner scaling for St. 6–12. Symbols from table 2. Lines: —— canonical ZPG comparison.

both inner and outer scalings are the same as those described for $\overline{u'^2}$ in figure 7. The profiles are suppressed toward a new equilibrium by the FPG, recover to match the canonical ZPG case by St. 9, and the peak grows rapidly in the APG. The dimensional value of the peak $-\overline{u'v'}$ in the outer region actually drops in the APG, so the rise in the profiles of figure 10 are entirely due to the drop in U_∞ and u_τ. Figure 11 shows the difference in outer coordinates between all cases of the present study and the canonical ZPG boundary layer at $y/\delta = 0.4$. The results are similar to those of $\overline{u'^2}$ in figure 8, and the same streamwise scaling of the streamwise distance is used. For the FPG, the Jones (1998) results for K of 0.27×10^{-6} and 0.539×10^{-6} approach an equilibrium value of approximately 5×10^{-4} in the coordinates of figure 11, which is roughly consistent with the most downstream results of the present cases in the same K range.

Quadrant analysis (Willmarth & Lu 1972) was used to further consider the effect of the pressure gradient. Within each quadrant, the response of the $-\overline{u'v'}$ profiles was essentially the same as for the composite $-\overline{u'v'}$ of figure 10. As expected, and in agreement with ZPG results, quadrants 2 (Q2, ejections, $u' < 0$, $v' > 0$) and 4 (Q4, sweeps, $u' > 0$, $v' < 0$) were most significant. At the y location where the Reynolds shear stress was largest, about twice as many events and four times the contribution
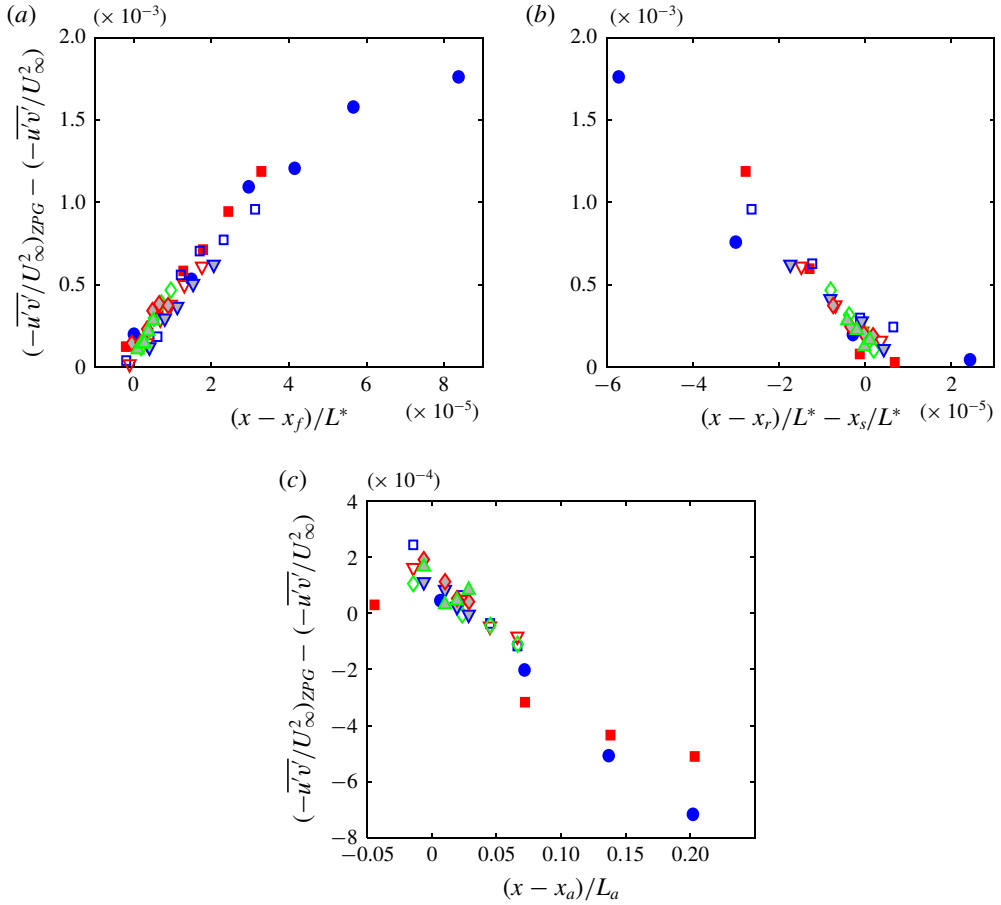
FIGURE 11. Difference between ZPG and non-ZPG $-\overline{u'v'}/U_\infty^2$ profiles at $y/\delta = 0.4$. ZPG and non-ZPG compared at same Re_θ. (a) FPG St. 1–6, (b) ZPG St. 6–9, (c) APG St. 9–12. Symbols from table 1.

to the Reynolds shear stress occurred in quadrants 2 and 4 than in quadrants 1 and 3, respectively. The pressure gradient caused changes in the relative contributions of Q2 and Q4. Profiles of the ratio of the contribution from Q2 to that from Q4 are shown in figure 12 for case 2. For the ZPG comparison cases, the ratio rises from the wall to a peak of about 1.2 at $y^+ \approx 30$. For locations very near the wall, there is little fluid even closer from which ejections can originate, so Q2 contributions are low. Farther out, Q2 and Q4 come more into balance and the ratio drops to near one. Beyond $y/\delta = 0.4$, the ratio rises as ejections remain significant but the intensity of sweeps decreases as the free stream is approached. Beyond $y/\delta = 1$ the ratio drops toward 1.0 as the turbulence becomes uncorrelated in the free stream and $u'v'$ has the same magnitude in all four quadrants. Volino (2020) found little variation in the Q2/Q4 ratio with Reynolds number for ZPG cases. For the non-ZPG cases, there is little change for $y^+ < 20$. In the middle of the boundary layer, the FPG causes the ratio to rise. The acceleration strains the turbulence in the outer flow, as shown above by the reduction in the Reynolds stresses and in the notional sketch in figure 13. This reduces the effect of sweeps. Ejections are still generated due to the high mean
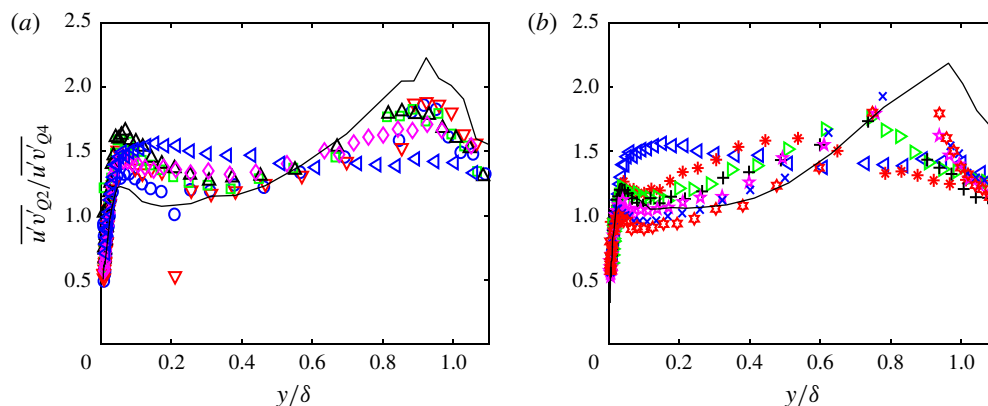
FIGURE 12. Profiles of the ratio of contributions to $\overline{u'v'}$ from Q2 and Q4 for case 2, (*a*) St. 1–6, (*b*) St. 6–12. Symbols from table 2. Lines: —— canonical ZPG comparison.
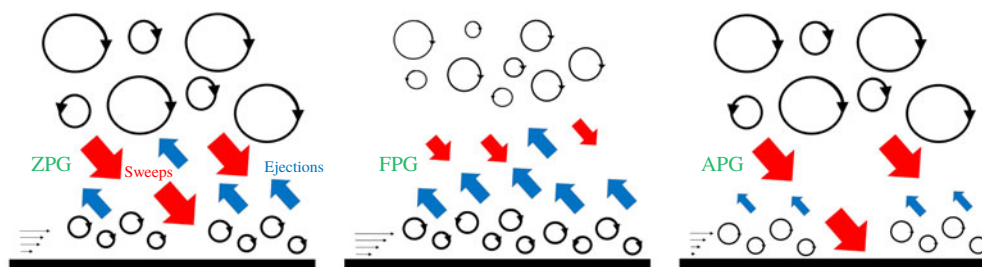
FIGURE 13. Notional drawing of the changes in turbulence in response to pressure gradients.

shear near the wall. The result is the rising Q2/Q4 ratio. In the recovery region, the ratio drops back to the canonical ZPG value. In the APG, the mean shear drops near the wall, reducing the near-wall turbulence and the strength of ejections. In the outer flow, the dimensional turbulence quantities do not change rapidly, as noted above, so sweeps from the outer region become more significant relative to ejections. The result is that the Q2/Q4 ratio drops below the ZPG profile. This is consistent with the DNS results of Lee & Sung (2009) and Lee (2017) and the growth of the inner $\overline{u'^2}$ peak in inner coordinates shown in figure 7(*d*). Case 1 showed the same behaviour as case 2. For the weaker ramp cases, the trends were less clear, which is consistent with the APG results of Lee (2017), who saw that the increasing strength of Q4 was most clear for cases with $\beta > 2.2$.

3.3. *Triple products*

The budget equations of the Reynolds stresses, as presented in references such as Reynolds (1976), are useful for understanding the development of turbulence. Many of the terms in the equations, including the dissipation terms and those involving pressure fluctuations, cannot typically be determined from experimental measurements. The triple products of the turbulent fluctuations, which are related to the transport of the Reynolds stresses, were measured and are considered next. Profiles of $\overline{u'^3}$ are shown in inner coordinates in figure 14 for case 2. There are two possible
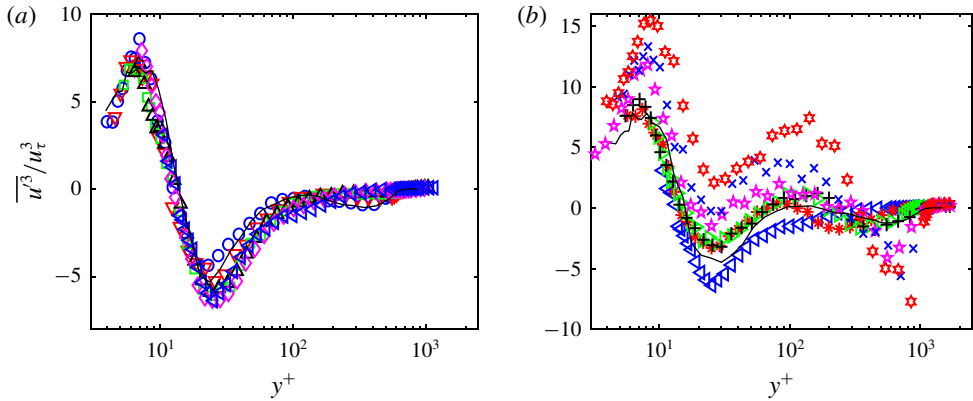
FIGURE 14. The $\overline{u'^3}$ profiles for case 2, (*a*) St. 1–6, (*b*) St. 6–12. Symbols from table 2. Lines: —— canonical ZPG comparison.

physical explanations for the turbulent transport associated with $\overline{u'^3}$. One is the streamwise transport of $\overline{u'^2}$ with u' fluctuations, but even with a mean pressure gradient, streamwise gradients are weak relative to wall-normal gradients, so there is little reason to expect significant streamwise turbulent transport. The other explanation is wall-normal transport of $\overline{u'^2}$ through the v' fluctuations associated with ejections and sweeps. Sweeps carry high speed fluid toward the wall, so they have positive u' and negative v'. Transport of $\overline{u'^2}$ with a sweep results in positive $\overline{u'^3}$ and negative $\overline{u'^2 v'}$ for the same event. Ejections correspondingly result in negative $\overline{u'^3}$ and positive $\overline{u'^2 v'}$. The behaviour in figure 14 is explained in terms of wall-normal motions. Transport toward the wall from the near-wall peak at $y^+ = 15$ in figure 7 results in the positive peak at $y^+ = 7$ in figure 14. Transport away from the wall produces the negative peak at $y^+ = 25$. In the FPG, since there is little change in the near-wall peak in $\overline{u'^2}$, there is little change in the near-wall peak in $\overline{u'^3}$. For the APG, the growth of the $\overline{u'^2}$ inner peak is reflected in the growth of the $\overline{u'^3}$ peak at $y^+ = 7$. The negative $\overline{u'^3}$ peak at $y^+ = 25$ grows in the FPG and then returns quickly to its original condition in the recovery region. This can be explained by the increased importance of ejections relative to sweeps at this location in the FPG shown in figure 12. The locations of the inner peaks are invariant with the pressure gradient, remaining at $y^+ = 7$ and 25 in all regions. This is consistent with the inner $\overline{u'^2}$ peak remaining at $y^+ = 15$.

In the outer region of the ZPG boundary layer, there is a small, broad negative peak in $\overline{u'^3}$ centred at $y/\delta = 0.6$. Its position varies with Reynolds number in inner coordinates, as shown for the ZPG cases in Volino (2020); it appears at $y^+ = 350$ at station 1 in figure 14(*a*). This peak is generated by transport of the outer region $\overline{u'^2}$ fluctuations, centred at $y^+ = 200$ in figure 7(*c*), toward the free stream. As these fluctuations are suppressed by the FPG, the corresponding $\overline{u'^3}$ is also suppressed. The outer region $\overline{u'^2}$ would also tend to produce a positive $\overline{u'^3}$ peak closer to the wall, but this effect appears to be overwhelmed by the effect of the larger near-wall peak in $\overline{u'^2}$. In the recovery region, the outer peaks in $\overline{u'^2}$ and $\overline{u'^3}$ quickly return to ZPG conditions. In the APG, as the outer peak in $\overline{u'^2}$, located at approximately $y/\delta = 0.35$, grows rapidly, the negative outer peak in $\overline{u'^3}$ at $y/\delta = 0.6$ does the same. As the outer $\overline{u'^2}$ peak grows, transport from it towards the wall causes a new positive peak in $\overline{u'^3}$ to
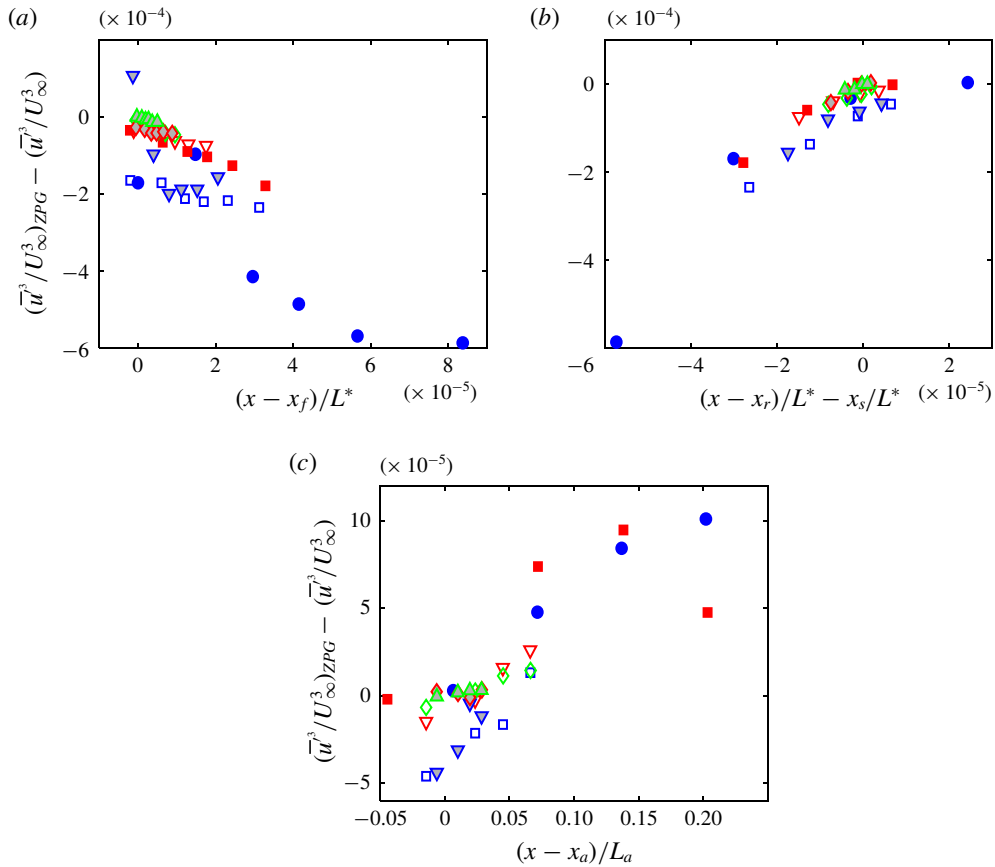
FIGURE 15. Difference between ZPG and non-ZPG $\overline{u'^3}/U_\infty^3$ profiles at $y/\delta = 0.6$. ZPG and non-ZPG compared at same Re_θ. (*a*) FPG St. 1, (*b*) ZPG St. 6–9, (*c*) APG St. 9–12. Symbols from table 1.

emerge centred at $y/\delta = 0.13$ ($y^+ \approx 110$ in figure 14*b*). The transport of outer region $\overline{u'^2}$ toward the wall begins to overwhelm the negative $\overline{u'^3}$ peak at $y^+ = 25$ and pull $\overline{u'^3}$ there up to positive values.

The changes in $\overline{u'^3}$ relative to the ZPG results are qualitatively the same for all cases, but of lower magnitude with milder pressure gradient. As an example, figure 15 shows the behaviour of the peak at $y/\delta = 0.6$ as a function of streamwise position in the format of figure 8. There is some scatter due to the uncertainty in the triple products, but the trend in each region is clear. Plots in the format of figure 15 are not included for the other peaks in $\overline{u'^3}$ or for the other triple products, but they exhibit similar behaviour.

As noted above, the triple product $\overline{u'^2 v'}$ also primarily results from the wall-normal transport of $\overline{u'^2}$, and exhibits the same behaviour as $\overline{u'^3}$. It is not shown here, but profiles are included in the Appendix for comparison.

Profiles of $\overline{v'^3}$, which is related to the wall-normal transport of $\overline{v'^2}$, are shown for case 2 in figure 16. The profiles are somewhat simpler than those of $\overline{u'^3}$ because $\overline{v'^2}$ has only a single peak, which is centred at approximately $y^+ = 100$ at station 1.
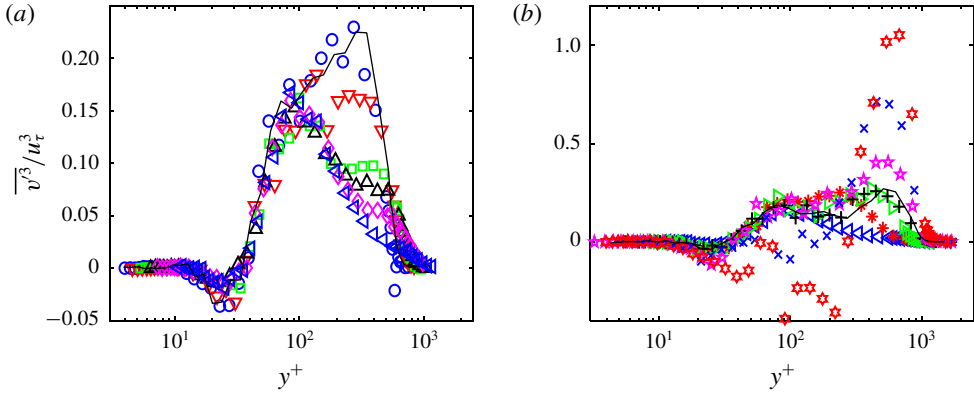
FIGURE 16. The $\overline{v'^3}$ profiles for case 2, (*a*) St. 1–6, (*b*) St. 6–12. Symbols from table 2. Lines: —— canonical ZPG comparison.

Transport from this peak towards the wall results in the small negative $\overline{v'^3}$ peak at $y^+ = 25$, and transport away from the wall causes the positive peak at $y^+ \approx 200$. The FPG suppresses $\overline{v'^2}$, particularly in the outer part of the flow, resulting in a corresponding reduction in magnitude of the $\overline{v'^3}$ peaks. In the recovery region the peaks increase in size, and the positive $\overline{v'^3}$ peak begins to split, with an inner peak near $y^+ = 100$ and an outer peak at $y^+ = 550$. The same splitting was observed with increasing Reynolds number in ZPG cases by Volino (2020), and is attributed to the broadening and flattening of the $\overline{v'^2}$ peak (shown in the Appendix and similar to the $-\overline{u'v'}$ peak of figure 10). At the centre of the $\overline{v'^3}$ peak there is some cancelation of the effects of the ejections and sweeps from either side of the $\overline{v'^2}$ peak, causing the dip at $y^+ = 300$. In the APG region, the rapid growth and shift to higher y^+ of $\overline{v'^2}$ results in a corresponding increase in magnitude of both the negative and positive $\overline{v'^3}$ peaks and a similar shift to higher y^+. The triple product $\overline{u'v'^2}$ is also related to the wall-normal transport of $\overline{v'^2}$, as carried by ejections and sweeps. It behaves similarly to $\overline{v'^3}$ and is show in the Appendix for comparison. The quantity $\overline{u'v'^2}$ can also be associated with the wall-normal transport of the Reynolds shear stress. Since the profiles of $\overline{v'^2}$ and $-\overline{u'v'}$ are similar, the same explanation of the $\overline{u'v'^2}$ behaviour can be applied to both $\overline{v'^2}$ and $-\overline{u'v'}$ transport.

3.4. *Production terms*

The production terms for the Reynolds stresses were also determined from the measurements. The production terms for $\overline{u'^2}$ are $-2\overline{u'v'}\partial U/\partial y$ and $-2\overline{u'^2}\partial U/\partial x$, as explained by Reynolds (1976). The former is the dominant term, at least for the present flows, since the gradient of the mean velocity is much stronger in the wall-normal direction than in the streamwise direction even for the strong pressure gradient cases. Profiles of $-2\overline{u'v'}\partial U/\partial y$ are shown in figure 17 for case 2 in inner coordinates. The peak at $y^+ = 11$ is suppressed slightly by the FPG, but the change is small, in agreement with the lack of change in the inner $\overline{u'^2}$ peak in figure 7. In the outer region, the values are low, but they are still noticeably reduced by the FPG. In the ZPG recovery, these trends are reversed, and the profile returns to match the canonical ZPG comparison case. In the APG, the inner peak grows, and an outer
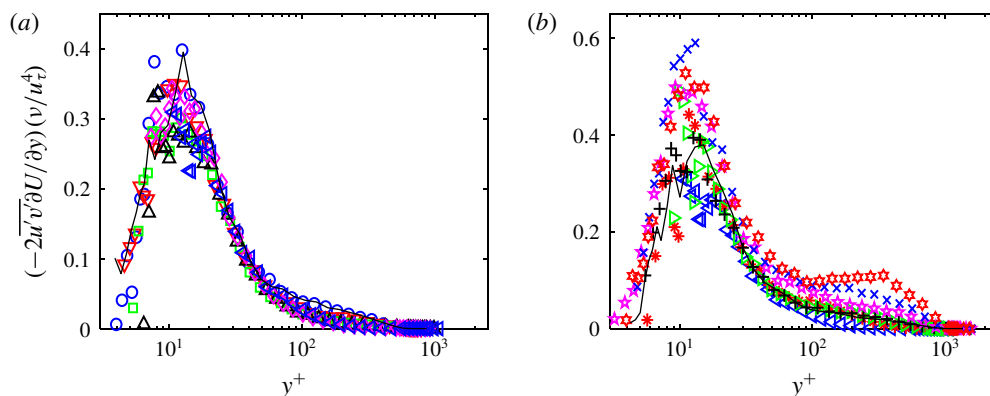
FIGURE 17. The $-2\overline{u'v'}\partial U/\partial y$ (production term for $\overline{u'^2}$) profiles for case 2, (*a*) St. 1–6, (*b*) St. 6–12. Symbols from table 2. Lines: —— canonical ZPG comparison.

peak centred at approximately $y^+ = 200$ emerges, again in agreement with the $\overline{u'^2}$ behaviour in figure 7. All cases exhibit the same behaviour shown in figure 17 for case 2. The changes in the inner peak are small, particularly for the weaker pressure gradient cases, and of the order of the uncertainty in the measurements. The location of the inner peak remains fixed at $y^+ = 11$ as the pressure gradient changes, which is consistent with fixed locations of the inner peaks in wall coordinates for all of the quantities considered above. The trends for the outer peak are clearest in outer scaling and are shown in figure 18 using the format of figure 8. Results are shown for the representative location $y/\delta = 0.4$, and are normalized as $(-2\overline{u'v'}\partial U/\partial y)(\delta/U_\infty^3)$. As in the quantities shown above, there is good agreement between all cases.

The production terms for $\overline{v'^2}$ are $-2\overline{u'v'}\partial V/\partial x$ and $-2\overline{v'^2}\partial V/\partial y$. The latter is the dominant term, but both are small compared to the dominant production terms in the $\overline{u'^2}$ and $-\overline{u'v'}$ budgets. As noted by Reynolds (1976), production of turbulent energy typically occurs first in some components of the Reynolds stress followed by transfer to others. The production terms for $-\overline{u'v'}$ are $\overline{u'^2}\partial V/\partial x$, $\overline{u'v'}\partial V/\partial y$, $\overline{u'v'}\partial U/\partial x$ and $\overline{v'^2}\partial U/\partial y$. Of these, the last is the dominant term. Profiles of it are shown in figure 19 in inner scaling for case 2. Similar to the results in figure 17, the entire profile is suppressed somewhat in the FPG region, recovers quickly in the ZPG recovery, and grows significantly in the APG. An inner peak is present at $y^+ = 15$, and an outer peak emerges in the APG, centred at about $y^+ = 300$. In outer scaling, the outer peak location is $y/\delta = 0.3$. Although not shown, all cases agree when presented in the format of figure 18. The changes in figure 19 correspond to those observed in $-\overline{u'v'}$ in figure 10.

3.5. *Spectra*

Additional velocity data were acquired with the LDV at a sufficiently high sampling rate for spectral analysis at each streamwise location of case 1 at $y/\delta = 0.15$ and 0.4. At each location, 240 s time records of instantaneous u and v were recorded in coincidence mode with average sampling rates of approximately 500 Hz at $y/\delta = 0.15$ and 700 Hz at $y/\delta = 0.4$. Data for spectral analysis were also acquired in the ZPG boundary layer at the same wall-normal locations at $Re_\theta = 1960$, 3600 and 6300 with an average sampling rate of about 1200 Hz. The dimensionless spectra for
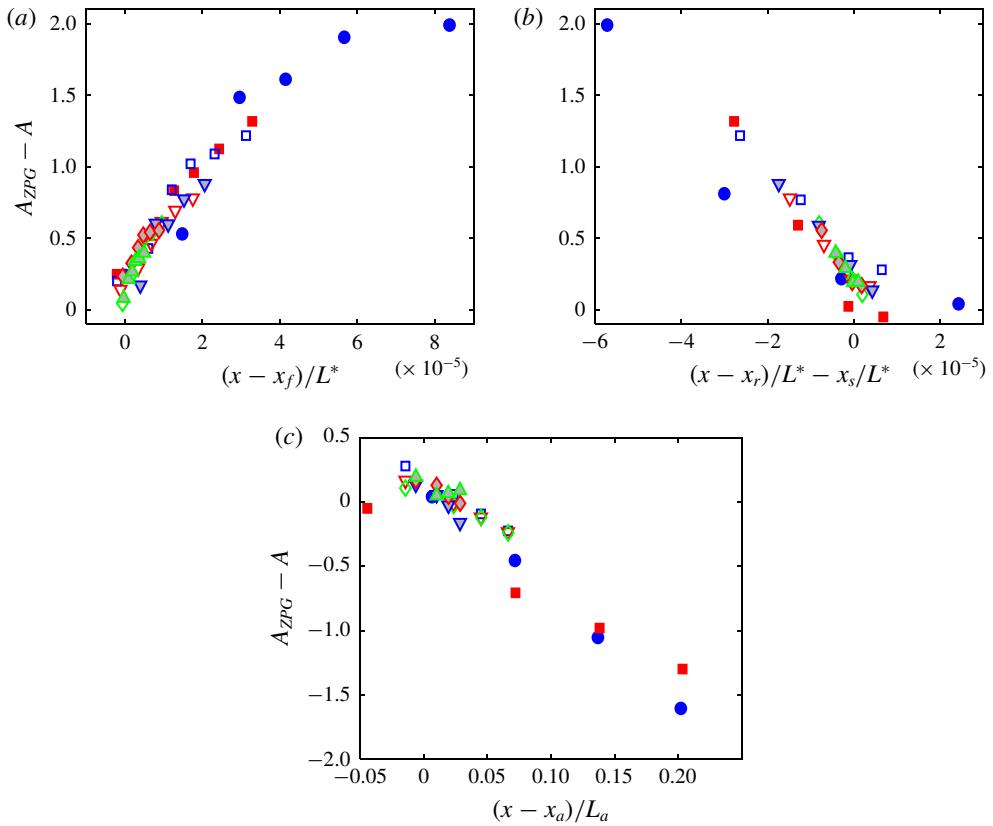
FIGURE 18. Difference between ZPG and non-ZPG profiles at $y/\delta = 0.4$. ZPG and non-ZPG compared at same Re_θ. $A = (-2\overline{u'v'}\partial U/\partial y)(\delta/U_\infty^3)$. (a) FPG St. 1–6, (b) ZPG St. 6–9, (c) APG St. 9–12. Symbols from table 1.
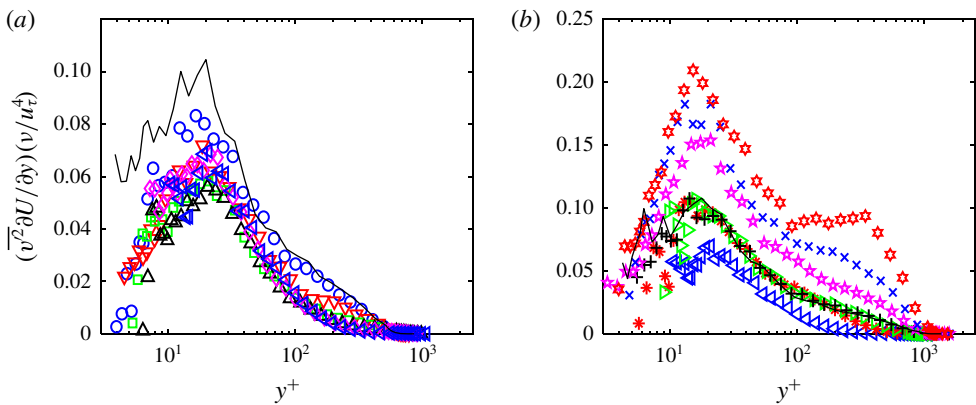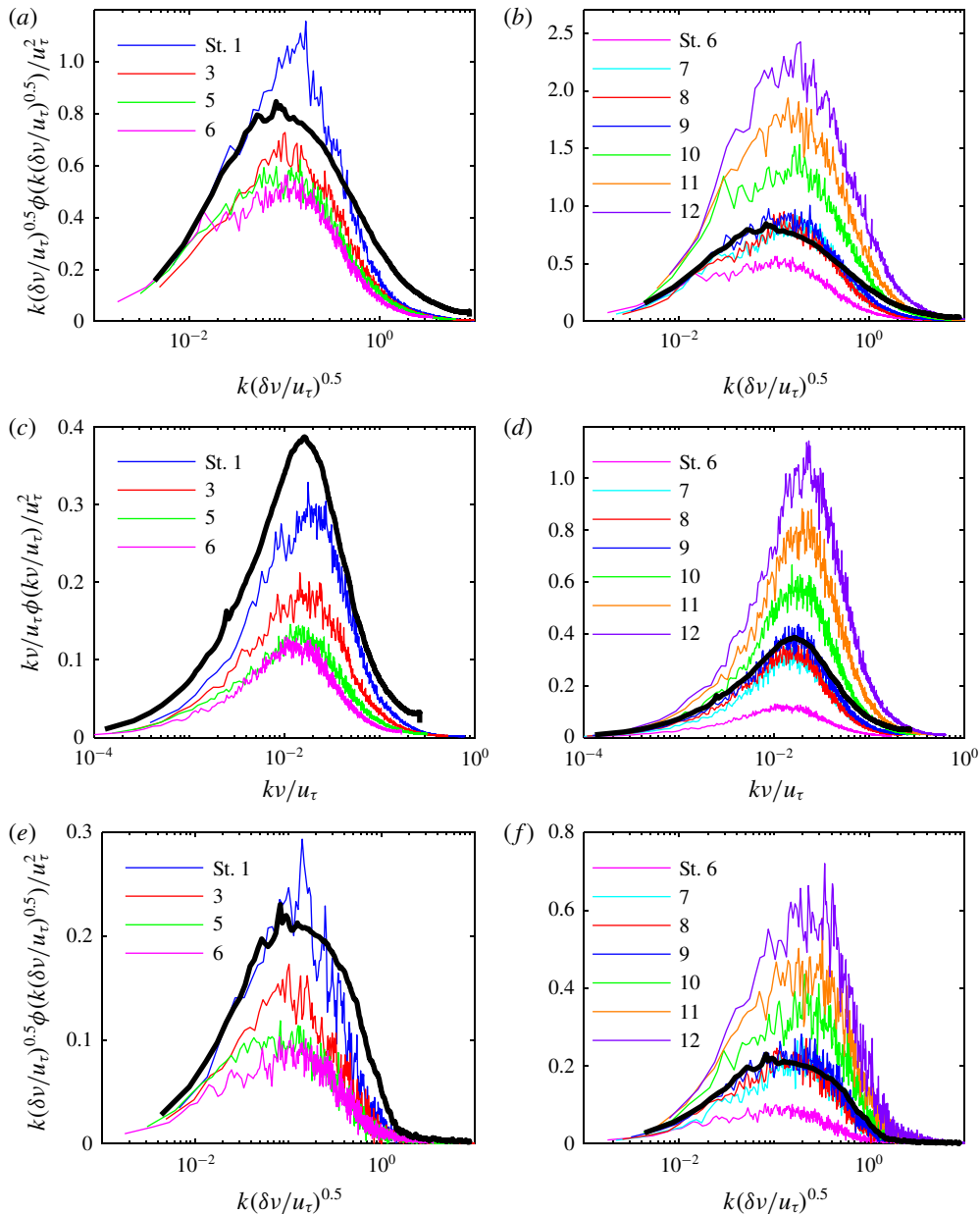

FIGURE 19. The $\overline{v'^2}\partial U/\partial y$ (production term for $-\overline{u'v'}$) profiles for case 2, (a) St. 1–6, (b) St. 6–12. Symbols from table 2. Lines: —— canonical ZPG comparison.

FIGURE 20. Premultiplied spectra of Reynolds stresses for case 1 at $y/\delta = 0.15$ (*a*) u'^2, St. 1–6, (*b*) u'^2, St. 6–12, (*c*) v'^2, St. 1–6, (*d*) v'^2, St. 6–12, (*e*) $u'v'$, St. 1–6, (*f*) $u'v'$, St. 6–12. Thick black line is smoothed, canonical ZPG comparison.

these ZPG cases were found to be invariant with Reynolds number. The spectra from the $Re_\theta = 3600$ case are used for comparison below. Premultiplied spectra of u'^2, v'^2 and $-u'v'$ at $y/\delta = 0.15$ are shown in figure 20. Frequencies were converted to wavenumbers, k, using the local mean streamwise velocity. Three different scalings were considered for the wavenumber. These were an outer scaling, $k\delta$, an inner scaling, $k\nu/u_\tau$, and a mixed scaling $k(\delta\nu/u_\tau)^{0.5}$. The latter is the meso
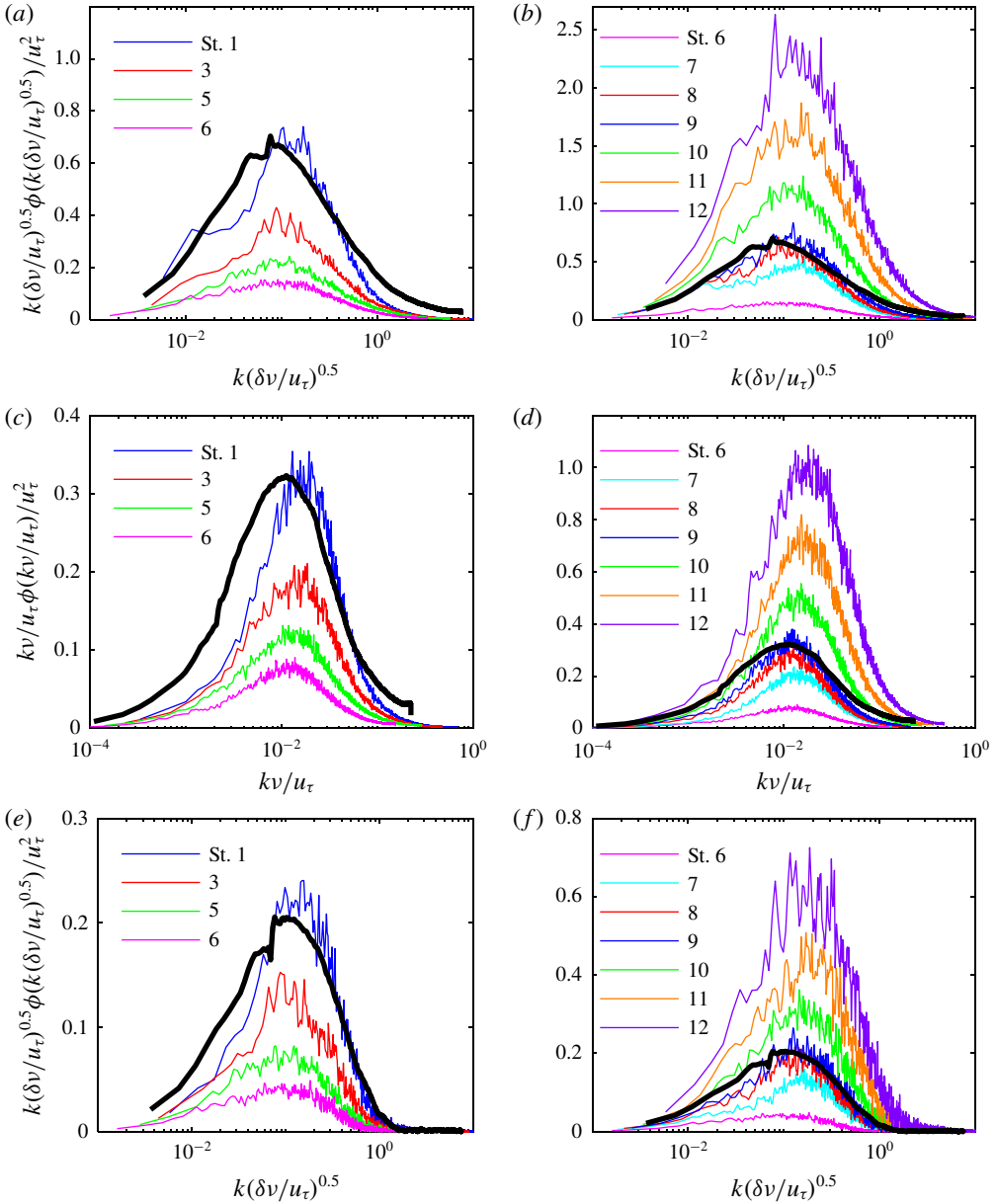
FIGURE 21. Premultiplied spectra of Reynolds stresses for case 1 at $y/\delta = 0.4$ (a) u'^2, St. 1–6, (b) u'^2, St. 6–12, (c) v'^2, St. 1–6, (d) v'^2, St. 6–12, (e) $u'v'$, St. 1–6, (f) $u'v'$, St. 6–12. Thick black line is smoothed, canonical ZPG comparison.

scale described in Wei *et al.* (2005). The inner scaling produced the best agreement through all regions for the v'^2 spectra, while the mixed scaling was best for u'^2 and $-u'v'$. These scalings are used in figures 20 and 21, and with these scalings there is little variation in the dimensionless wavenumber of the spectral peaks through all three regions. The magnitudes of the peaks do not collapse with any scaling and cannot be expected to. In premultiplied coordinates, the area under each spectrum

is equal to the respective Reynolds stress, and the Reynolds stresses clearly change in response to the pressure gradients as shown above. At station 1, the spectra of the present case are similar to those of the ZPG comparison case (shown smoothed with a thick black line). The FPG suppresses the turbulence across the entire spectra. As in the mean Reynolds stresses, the recovery to ZPG conditions is rapid. At the end of the recovery the spectra agree well with the ZPG baseline. In the APG, there is continuous growth in the spectra magnitude across all wavenumbers for all quantities. The spectra at $y/\delta = 0.4$, shown in figure 21, are very similar to those at $y/\delta = 0.15$ in terms of wavenumber and magnitude. There is a noticeable difference, however, in the response to the FPG and ZPG recovery. At $y/\delta = 0.15$, the approach to equilibrium is more rapid, with the spectra at stations 5 and 6 agreeing well with each other, and the station 3 spectra not greatly different. At $y/\delta = 0.4$ there is more separation between the spectra at these stations. The same is true in the recovery. The spectra at stations 7–9 collapse at $y/\delta = 0.15$, but the recovery is somewhat more gradual at $y/\delta = 0.4$, with the station 7 spectra distinct from those at stations 8 and 9. The difference in the responses at $y/\delta = 0.15$ and 0.4 is consistent with the above discussion of the turbulence statistics. Closer to the wall the turbulence is generated primarily through the mean shear and responds more directly to the change in mean velocity. Farther from the wall, there is more of a lag as the rest of the boundary layer responds to the near-wall change.

3.6. *Turbulence structure, x–y plane*

The turbulence structure in the x–y plane is illustrated using linear stochastic estimation (LSE). The technique as used here is explained in Volino, Schultz & Flack (2009), and is similar to that used by Hambleton, Hutchins & Marusic (2006) and Christensen & Adrian (2001), based on the derivation of Adrian & Moin (1988). In LSE, the average velocity field associated with a conditioning event is computed. Whenever the conditioning event occurred, the instantaneous fluctuating velocity field at locations Δx and Δy from the event was identified. Streamwise averaging was then done among all locations with the same Δx and Δy in the field, and then over the 1000 vector fields acquired. Prograde swirl at a specified distance, y_{ref}, from the wall was used as the conditioning event in the x–y plane, as in Volino *et al.* (2009). Swirl strength, λ, was defined by Zhou *et al.* (1999) as the imaginary part of the complex eigenvalue of the local velocity gradient tensor. It is closely related to the vorticity resulting from rotation, as opposed to pure shear. It was used in the present context in a two-dimensional form, as explained in Volino *et al.* (2009) and Hutchins, Hambleton & Marusic (2005). Prograde swirl, as used by Wu & Christensen (2006), refers to vortices rotating in the direction of hairpin vortex heads, which is the direction induced by the mean shear. The LSE result can be associated with the hairpin packet surrounding the conditioning event. Figure 22 shows the LSE results for case 2 at stations 1, 6, 9 and 12 at the ends of the ZPG development, FPG, ZPG recovery and APG regions, respectively. Each vector is normalized for presentation by its own magnitude to prevent those closest to the reference point from dominating the field. The arrows, therefore, are all the same length and indicate only direction. The conditioning event was at $y_{ref}/\delta = 0.4$, and a clear clockwise (prograde) vortex appears at this location. Areas of organized vectors indicate correlation with the conditioning event, while regions with random appearing vectors are uncorrelated. The fields at stations 1 and 9 are very similar to the canonical ZPG result in Volino *et al.* (2009). A 'crease' extends both upstream and downstream from the reference
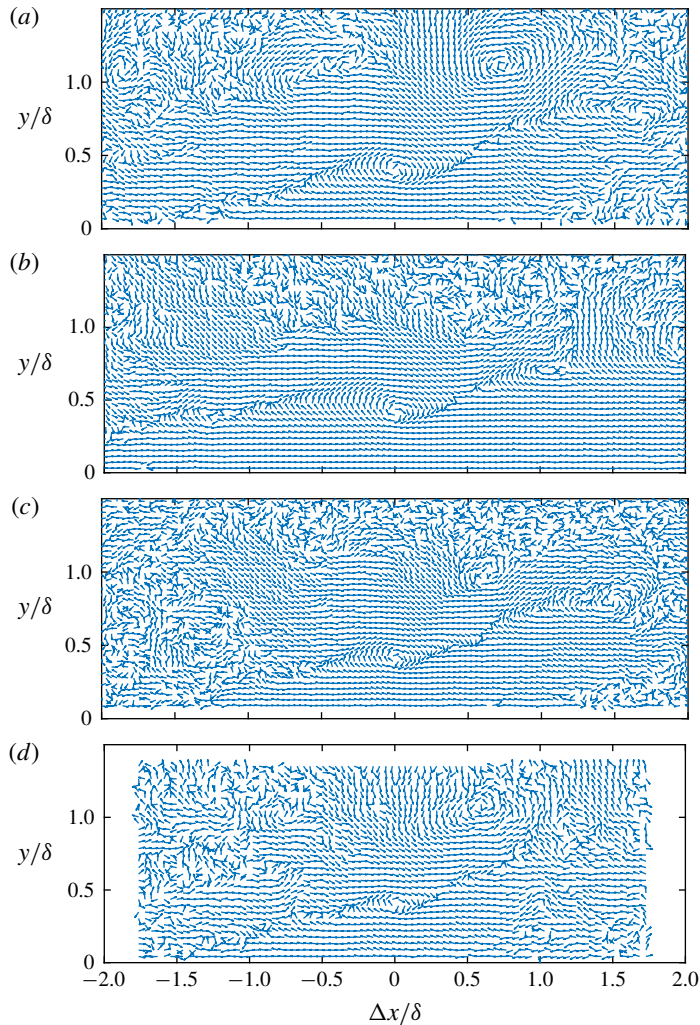
FIGURE 22. LSE conditioned on prograde swirl events at $y/\delta = 0.4$ for case 2, (*a*) St. 1, (*b*) St. 6, (*c*) St. 9, (*d*) St. 12.

point inclined at about 14° to the wall. Prograde rotations appear along the crease, spaced roughly δ apart, suggesting other hairpins associated with the same packet. Below the crease the vectors induced by the vortices generally point upstream and toward the crease (Q2 motions), while above the crease they are directed downstream and toward the crease (Q4 motions). The streamwise extent of the organized region is about $-1.2 < \Delta x/\delta < 1.5$, and the wall-normal range extends from the wall to about $y/\delta = 1$. The FPG clearly changes the LSE field, particularly below the reference point. The inclination angle of the crease upstream of the reference point is reduced to about 6°. The correlated region below the reference point is longer and extends beyond the field of view. Some of the increase in streamwise extent is due to the reduction in the normalizing quantity δ, and some is due to a dimensional increase in the size of the region. In the APG region, the streamwise length of the correlated region is reduced somewhat relative to the ZPG result, particularly downstream of the reference point. The inclination angle of the crease increases slightly to about 17°.
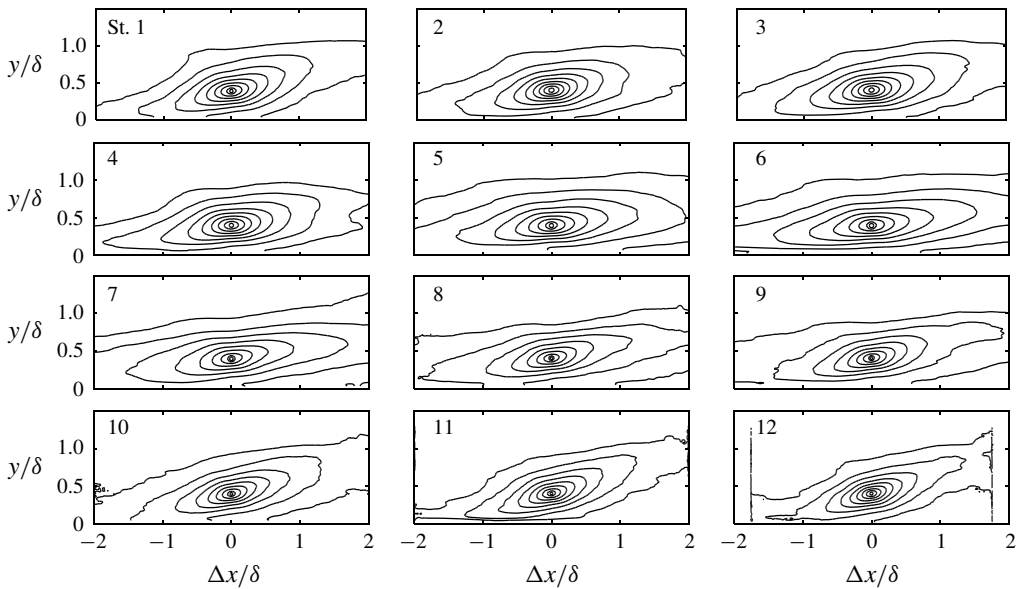
FIGURE 23. Contours of R_{uu} centred at $y/\delta = 0.4$ for 12 stations of case 2, outermost contour $R_{uu} = 0.1$, contour spacing 0.1.

In all regions, there is little change in the wall-normal extent of the correlated region. The trends with pressure gradient are similar when other distances from the wall are used as reference locations. The LSE results for case 1 were very similar to those shown for case 2. With the weaker ramps of cases 3–8, the trends with pressure gradient were similar, but less pronounced, as shown below.

Two-point correlations of the turbulence quantities were used to further quantify the pressure gradient effects. In the x–y plane, the correlation, as explained in Volino *et al.* (2007), is defined as

$$R_{AB}(y_{ref}) = \frac{\overline{A(x, y_{ref})B(x + \Delta x, y_{ref} + \Delta y)}}{\sigma_A(y_{ref})\sigma_B(y_{ref} + \Delta y)}, \tag{3.1}$$

where A and B are the quantities of interest at two locations separated in the streamwise and wall-normal directions by Δx and Δy, and σ_A and σ_B are the standard deviations of A and B at y_{ref} and $y_{ref} + \Delta y$, respectively. At every y_{ref}, the overbar indicates the correlations were averaged among locations with the same Δx and Δy, and then time averaged over the 1000 vector fields acquired. Figure 23 shows contours of the streamwise fluctuating velocity correlation, R_{uu}, with the correlation centred at $y_{ref}/\delta = 0.4$ for all stations of case 2. At station 1, the shape and extent of the contours agree with the ZPG results in the literature, such as those in Volino *et al.* (2007). The correlated region shown can be associated with the extent of a hairpin packet. In the FPG region, the streamwise extent of the contours increases and the inclination angle of the contours with respect to the wall is reduced, in agreement with the LSE results of figure 22. In the recovery region the trends are reversed, and the extent of the contours return to values similar to those at station 1. In the APG region the streamwise extent of the contours is decreased somewhat, and the inclination angle appears to increase. These trends are more clearly illustrated
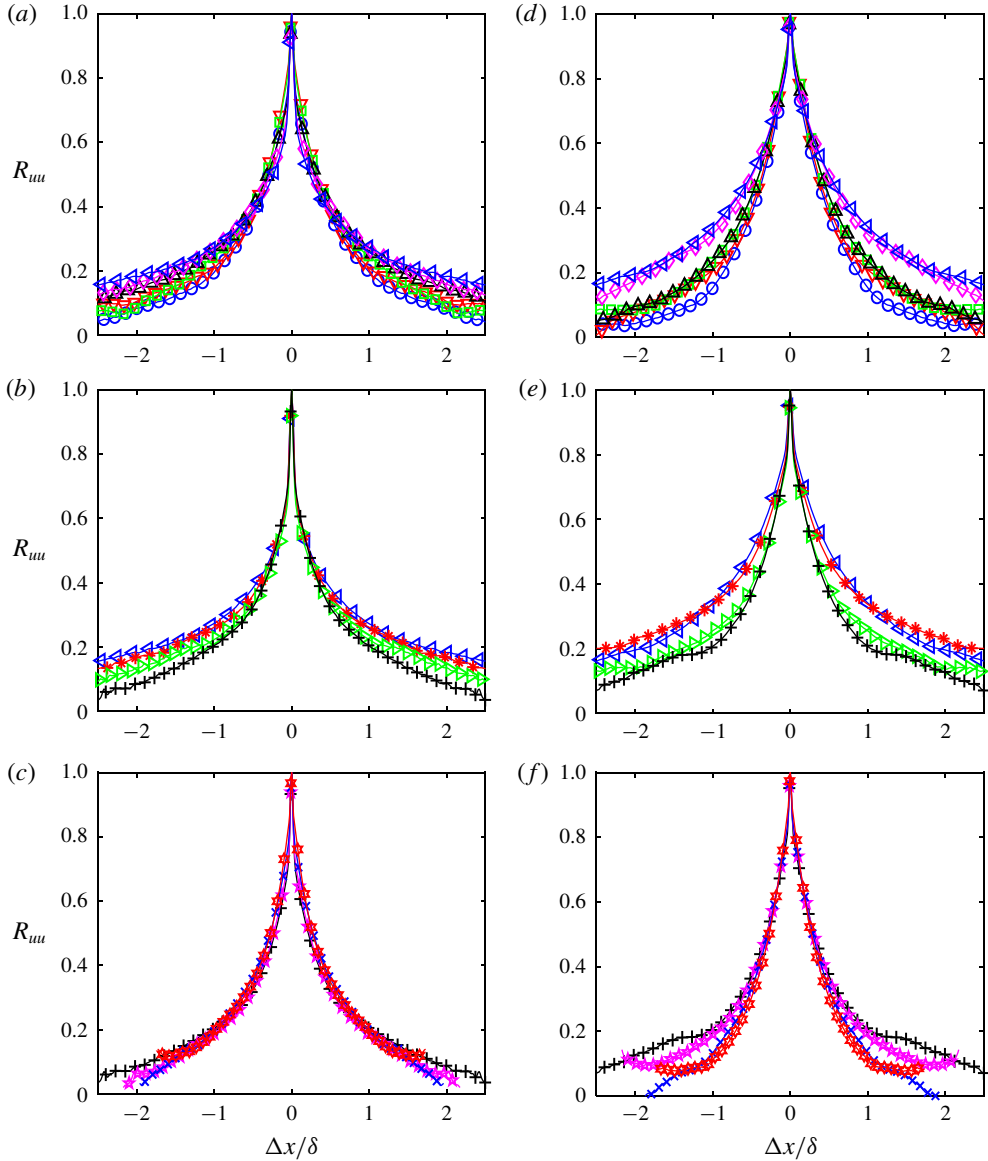
FIGURE 24. Streamwise slices through self-correlation point of R_{uu} of case 2, (*a*) centred at $y/\delta = 0.15$, St. 1–6, (*b*) $y/\delta = 0.15$, St. 6–9, (*c*) $y/\delta = 0.15$, St. 9–12, (*d*) $y/\delta = 0.4$, St. 1–6, (*e*) $y/\delta = 0.4$, St. 6–9, (*f*) $y/\delta = 0.4$, St. 9–12. Symbols from table 2.

in figure 24, which shows streamwise cuts through the self-correlation point for $y_{ref}/\delta = 0.15$ and 0.4. The increase in streamwise extent is clear in the FPG at both distances from the wall, as is the reversal in the ZPG recovery. There is little change in the APG region. Wall-normal cuts (not shown) through the centre of the R_{uu} contours show little change with pressure gradient at either y_{ref} location and agree with the ZPG results in Volino *et al.* (2007).

The inclination angle, θ_{uu}, of R_{uu} was determined, as in Volino *et al.* (2007) using a least squares fit to a line through the points farthest, both upstream and downstream,
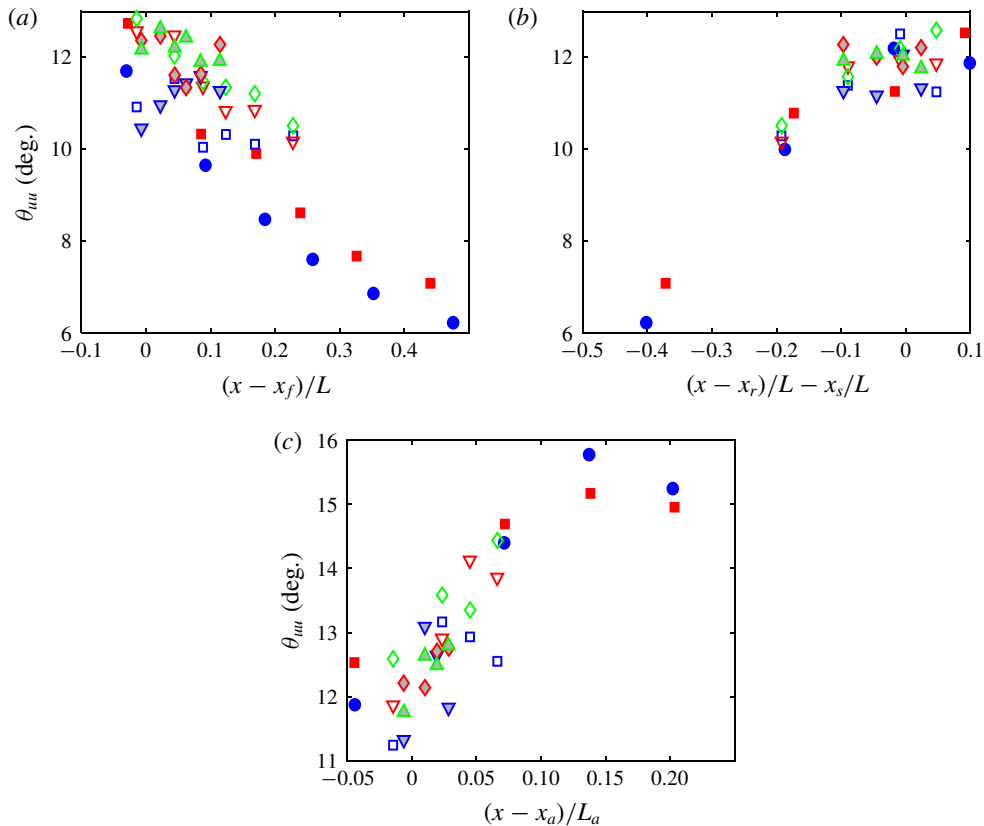
FIGURE 25. Average inclination angle of R_{uu} contours, (*a*) FPG St. 1–6, (*b*) ZPG St. 6–9, (*c*) APG St. 9–12. Symbols from table 1.

from the self-correlation peak on each of the $R_{uu} = 0.5, 0.6, 0.7, 0.8$ and 0.9 contours. As in Volino *et al.* (2007), the angle showed little variation for y_{ref}/δ between 0.2 and 0.7 and is presented next as an average of the values determined between these limits. Figure 25 shows the variation of θ_{uu} with streamwise location for all cases in the format of figure 3. The inclination angle is about 12° in the ZPG, in agreement with Volino *et al.* (2007) and other results in the literature. It drops toward about 7° in the FPG, progressing farther for the ramp 1 cases since these cases extend farther in the streamwise direction toward the sink flow length. The ZPG recovery is rapid, and the angle returns to 12°. In the APG, the angle increases to about 15°. The angles obtained from R_{uu} agree well with those estimated from the LSE results of figure 22. The increase in the inclination angle in the APG is consistent with the results of Lee & Sung (2009), who reported an angle of about 18° in an equilibrium APG with $\beta = 1.68$. At higher β the present angles are significantly lower than those reported by Lee (2017) for equilibrium cases, possibly indicating that the angles of the present cases might continue to increase if the streamwise development length were longer.

The streamwise length, Lx_{uu}, is defined as in Christensen & Wu (2005) as twice the distance from the self-correlation peak to the most downstream location on the $R_{uu} = 0.5$ contour. As with θ_{uu}, there was little variation between $0.2 < y_{ref}/\delta < 0.7$, and the average for this range is presented for all cases as a function of streamwise
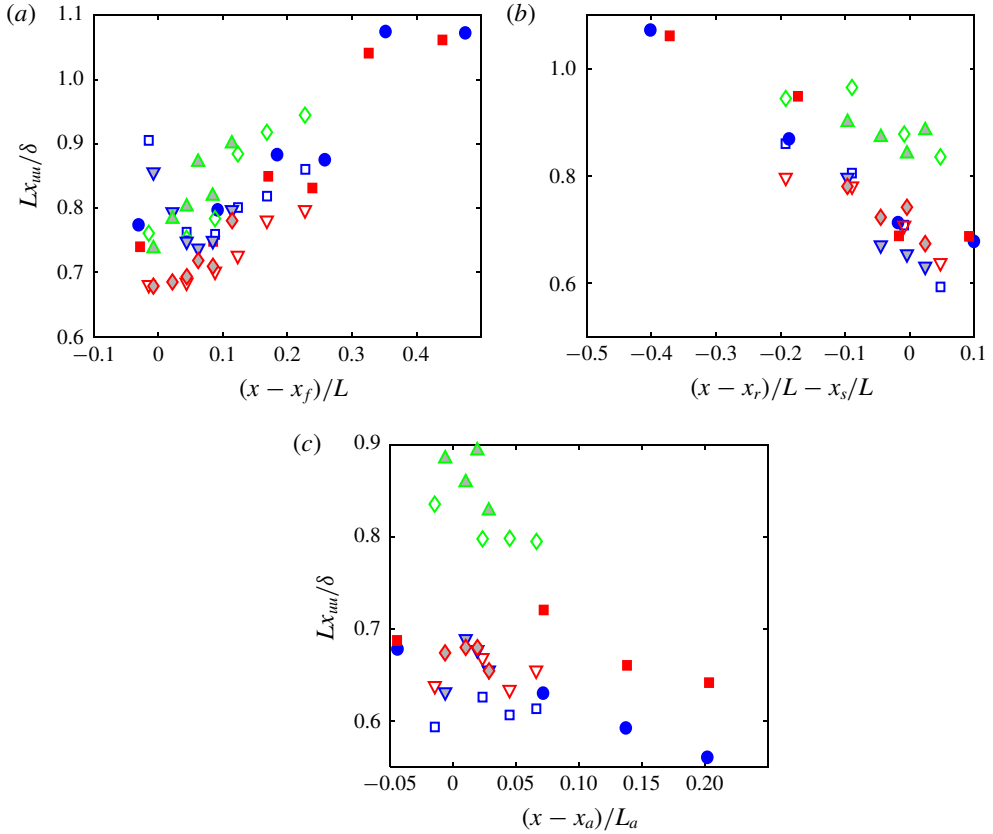
FIGURE 26. Average streamwise extent of $R_{uu} = 0.5$ contour, (*a*) FPG St. 1–6, (*b*) ZPG St. 6–9, (*c*) APG St. 9–12. Symbols from table 1.

position in figure 26. There is scatter in the results, which is most noticeable in the APG region since the overall changes were small, but the trends for all cases agree with the observations for case 2 in figures 23 and 24. The wall-normal length, Ly_{uu}, is defined as the wall-normal distance between the points closest and farthest from the self-correlation point on the $R_{uu} = 0.5$ contour. In the strongest pressure gradient cases it generally followed the same trends as Lx_{uu}, but differed by only approximately 10 % from the ZPG value, as might be expected based on figure 23. The increased streamwise length and decreased inclination of the structures in the FPG could be interpreted to result from streamwise stretching caused by the acceleration. Another possible explanation is the decreased outer region turbulence and the reduced impact of Q4 events noted above. With less disturbance from above, coherent regions closer to the wall may persist longer in the streamwise direction.

Examples of the correlations of other turbulence quantities are shown in figure 27. Included are contours of R_{vv} and the cross-correlations R_{uv}, $R_{\lambda u}$, and $R_{\lambda v}$ for stations 1, 6, 9 and 12 of case 2. The R_{vv} and $R_{\lambda v}$ correlations, which do not involve the streamwise component of the velocity, showed some indication of an increase in spatial extent in the FPG region and a reverse in the ZPG recovery, similar to R_{uu}, but the trend was not strong and not consistent between cases. The R_{vv} contours do not exhibit an inclination with respect to the wall, in contrast to R_{uu}. The $R_{\lambda v}$ contours can be associated with the head of a hairpin vortex (prograde swirl) at
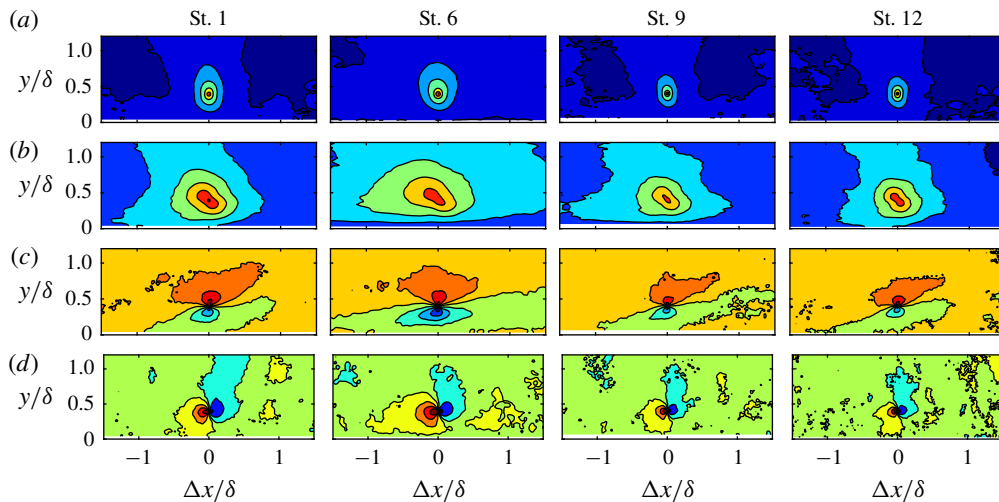
FIGURE 27. Contours of correlations for case 2, (*a*) R_{vv}, innermost contour $R_{vv} = 0.8$, contour spacing 0.2, (*b*) R_{uv}, innermost contour $R_{uv} = -0.45$, contour spacing 0.1, (*c*) $R_{\lambda u}$, outermost contours $R_{\lambda u} = \pm 0.015$, contour spacing 0.04, (*d*) $R_{\lambda v}$, outermost contours $R_{\lambda v} = \pm 0.01$, contour spacing 0.04.

the centre of the correlation. Fluid is pulled away from the wall on the upstream side and directed toward the wall on the downstream side. One noticeable effect of the pressure gradient on $R_{\lambda v}$ is the larger extent of the negatively correlated region upstream and below the correlation point in the FPG. This would suggest a greater impact of ejections (Q2) related to sweeps (Q4) in the FPG, in agreement with the quadrant analysis results shown above.

The trends with pressure gradient were clearer for R_{uv} and $R_{\lambda u}$, which do involve u'. The R_{uv} contours were inclined at a negative angle with respect to the wall, as might be expected for Q2 and Q4 events. The angle, θ_{uv} was quantified using a least squares fit to define a line though the upstream and downstream points farthest from the centre of the correlation on the -0.3 and -0.35 contours, and is shown in figure 28 in the coordinates of figure 25. Similar to R_{uu}, the magnitude of the inclination angle was reduced in the FPG, starting from an initial value of about $-36°$ and approaching an equilibrium of about $-22°$ at $(x - x_f)/L = 0.25$ in case 1. Although there is scatter in the results, the trend is the same for all cases and the change in angle is lower for the weaker K cases. The FPG was followed by a return to the ZPG value of approximately $-36°$ by the end of the recovery region, and a slight additional increase in magnitude in the APG. The streamwise extent of the correlation, Lx_{uv}, was defined as the distance between the most upstream and downstream points on the $R_{uv} = -0.3$ contour. It also followed the behaviour of R_{uu}, increasing in the FPG, dropping back to the original value in the recovery, and dropping slightly more in the APG. The percentage change in the length and the streamwise distance in which it occurred were essentially the same as shown for θ_{uv} in figure 28. The wall-normal distance, Ly_{uv}, which was also based on the -0.3 contour, behaved similarly, but as with R_{uu}, the changes were small.

The correlation $R_{\lambda u}$, as with $R_{\lambda v}$, can be associated with the head of a hairpin vortex. Fluid is directed downstream above the centre of the correlation and upstream below, as shown in the LSE results of figure 22. The changes with pressure gradient are the same as those of R_{uu}. The inclination of the line between the positively and negatively
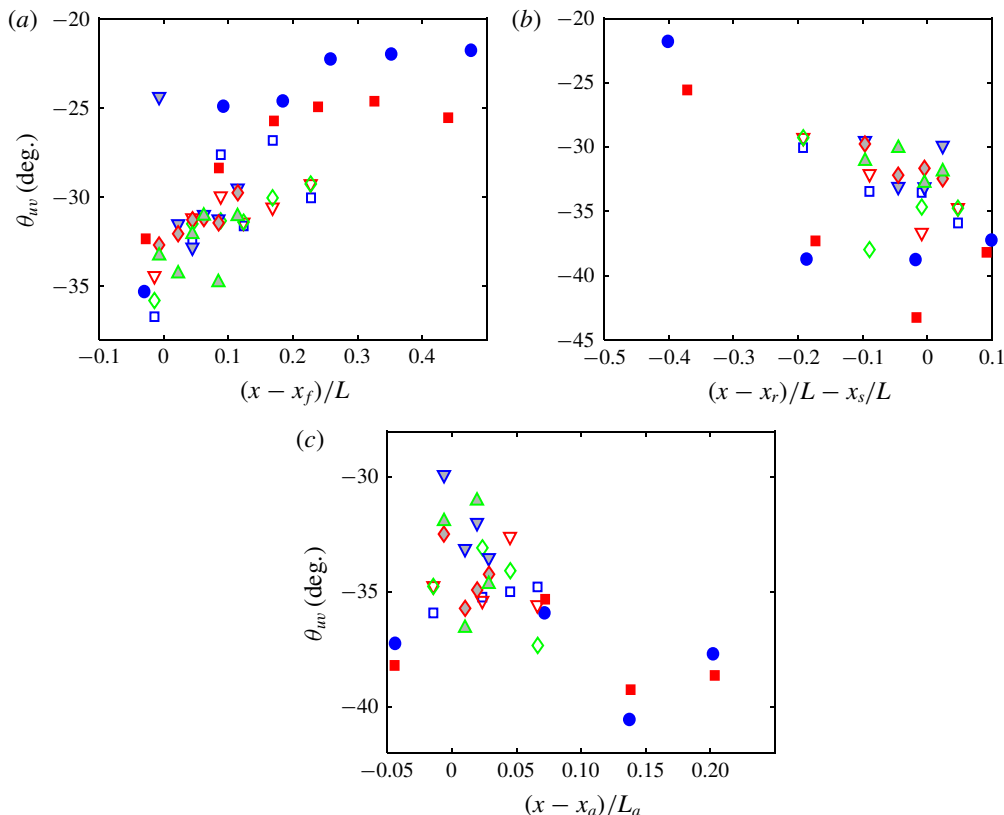
FIGURE 28. Average inclination angle of R_{uv} contours, (*a*) FPG St. 1–6, (*b*) ZPG St. 6–9, (*c*) APG St. 9–12. Symbols from table 1.

correlated region of $R_{\lambda u}$ decreases with the FPG, and then increases in the recovery and APG regions. The streamwise extent of the correlation, particularly between the correlation centre and the wall, increases with the FPG and then drops in the following regions. These results again agree with those of figure 22. The APG results are very similar to the equilibrium APG DNS results of Lee & Sung (2009) and Lee (2017). In particular, they noted the decreased extent of the negative $R_{\lambda u}$ contours downstream and below the correlation centre, and attributed it to the increased sweep influence as Q4 became larger relative to Q2.

3.7. *Turbulence structure, x–z plane*

The turbulence structure in the *x–z* plane, as shown in studies such as Volino *et al.* (2007) and Hutchins *et al.* (2005) is characterized by high and low speed streaks. This is illustrated in figure 29, which shows LSE results for station 9 of case 2 at $y/\delta = 0.4$. Clockwise swirl, in the view of the figure, at any location in the plane was used as the conditioning event. Streamwise, spanwise and time averaging were done among all locations with the same Δx and Δz spacings. The conditioning event can be associated with one leg of a hairpin vortex. Although cane vortices, consisting of only a single leg as opposed to a fully formed hairpin, might be present in the instantaneous flow, in the average that LSE shows, the leg of a hairpin should be accompanied by the
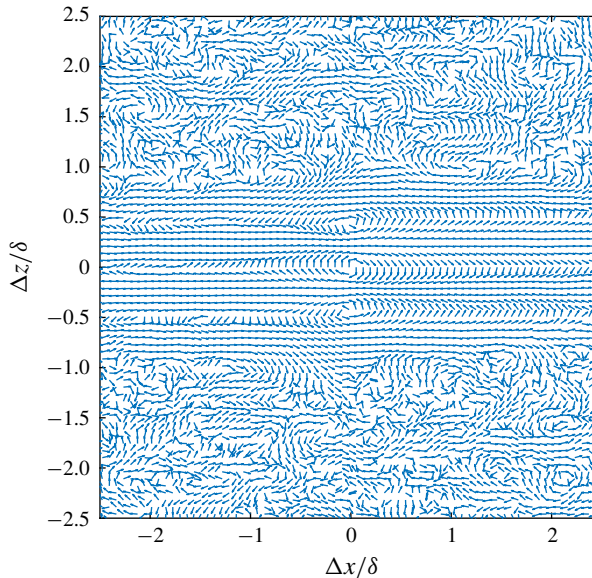
FIGURE 29. LSE conditioned on clockwise swirl events at $y/\delta = 0.4$ for St. 9 of case 2.

opposite leg. This is seen in figure 29 as oppositely rotating vortices spaced at about $\Delta z/\delta = \pm 0.5$ from the conditioning vortex at the centre of the field. Between the vortices are high and low speed streaks of positive and negative u' induced by the vortices. These streaks extend the full length of the field of view. All the LSE results in the x–z plane were qualitatively similar, but the spanwise spacing of the vortices varied. This spacing is shown as a function of streamwise position for all stations of all cases in figure 30 for planes at $y/\delta = 0.15$ and 0.4. At $y/\delta = 0.15$ there is a trend of increased spacing in the FPG and a return to the original ZPG value in the recovery, but with the exception of station 6 in the ramp 1 cases, the changes are small relative to the scatter in the data.

In the APG the decrease in the spacing continues. The vortex spacing is approximately 30 % larger at $y/\delta = 0.4$ than at $y/\delta = 0.15$. In agreement with the statistics shown above, the effect of the pressure gradient is stronger farther from the wall, and at $y/\delta = 0.4$ the changes in the vortex spacing are larger than at $y/\delta = 0.15$. The vortex spacing nearly doubles in the FPG for the ramp 1 cases and returns to its original value in the recovery. It decreases another 20 % in the APG. Changes are smaller for the ramp 2 and 3 cases, but the trends are the same.

Two-point correlations in the x–z plane are defined as

$$R_{AB} = \frac{\overline{A(x, z)B(x + \Delta x, z + \Delta z)}}{\sigma_A \sigma_B}, \qquad (3.2)$$

where A and B are the quantities of interest at two locations separated by Δx and Δz, and σ_A and σ_B are the standard deviations of A and B based on data in the full measurement plane for the 1000 vector fields acquired. Streamwise, spanwise and time averaging were done for all location pairs with the same Δx and Δz. Contours of the correlations R_{uu}, R_{ww}, $R_{\lambda u}$ and $R_{\lambda w}$ are shown in figure 31 for stations 1, 6, 9 and 12 of case 2 at $y/\delta = 0.4$. In the FPG region, the correlated regions of all quantities
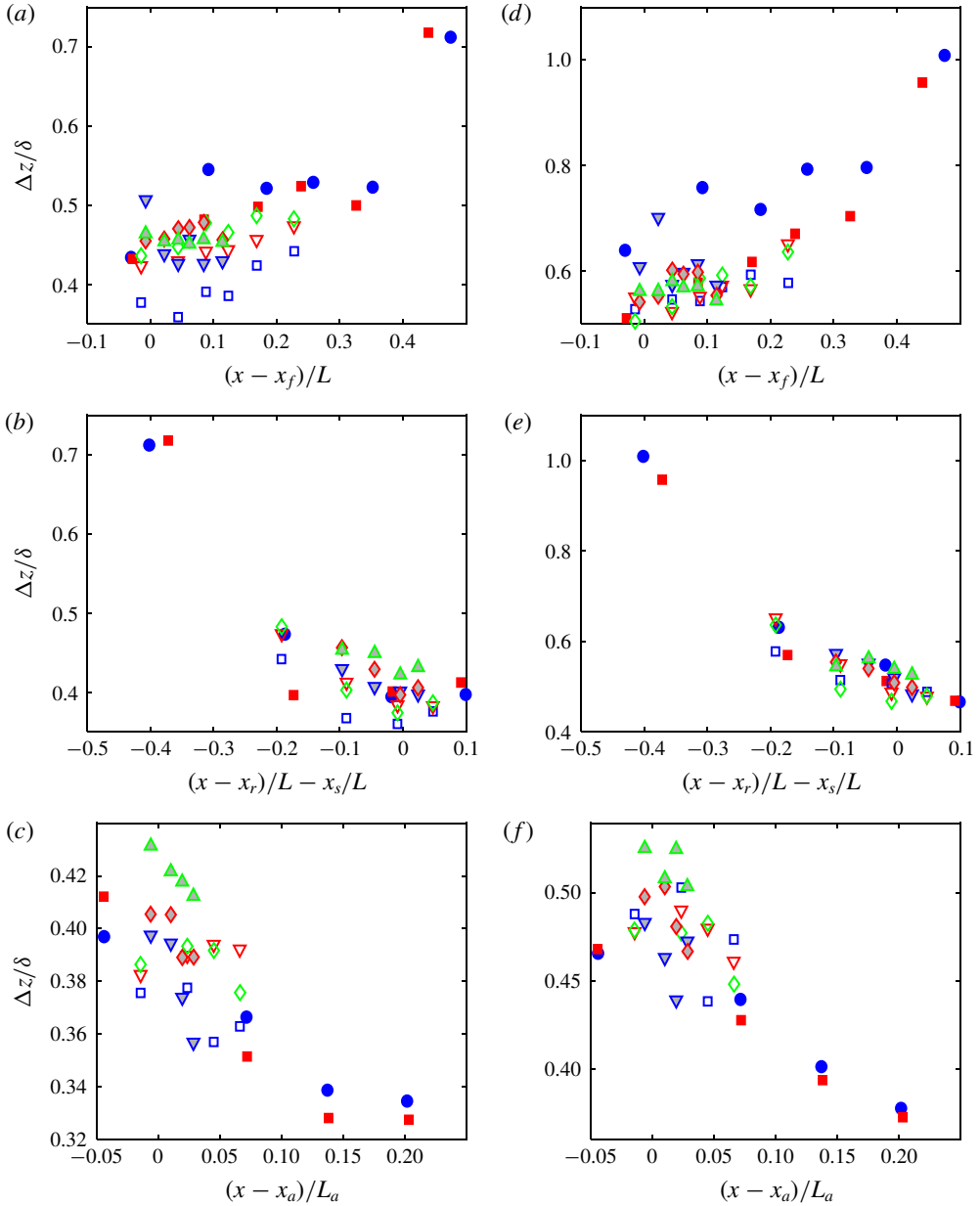
FIGURE 30. Spacing between vortices identified using LSE in *x*–*z* plane (as in figure 29), (*a*) at $y/\delta = 0.15$, FPG St. 1–6, (*b*) $y/\delta = 0.15$, ZPG St. 6–9, (*c*) $y/\delta = 0.15$, APG St. 9–12, (*d*) at $y/\delta = 0.4$, FPG St. 1–6, (*e*) $y/\delta = 0.4$, ZPG St. 6–9, (*f*) $y/\delta = 0.4$, APG St. 9–12. Symbols from table 1.

increase in size relative to δ in both the streamwise and spanwise directions. In the recovery region, there is a rapid return to the original size. Little change is seen in the APG region, indicating that the structures are growing proportionally with δ. The changes are illustrated with cuts through the correlation contours. Streamwise cuts through the centre of the R_{uu} correlation provide the same information and match
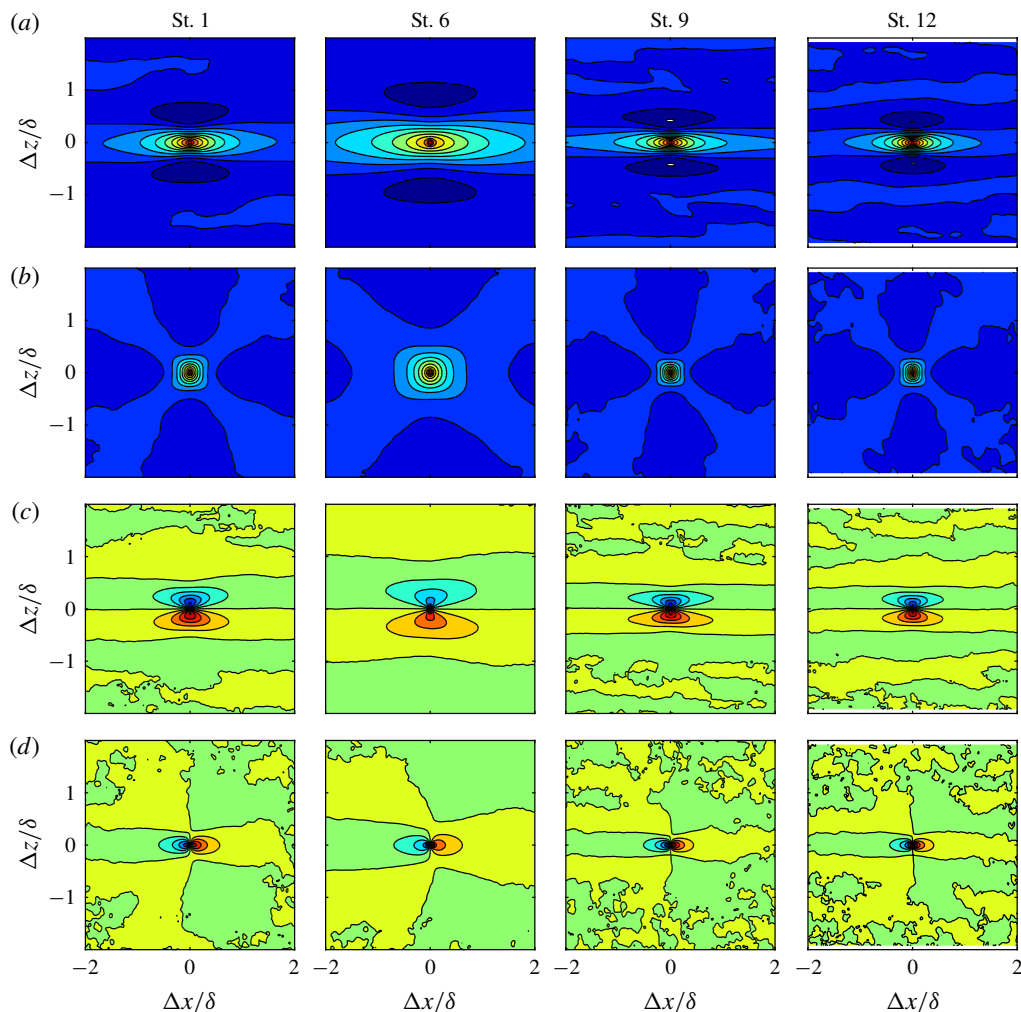
FIGURE 31. Contours of correlations for case 2 at $y/\delta = 0.4$, (a) R_{uu}, innermost contour $R_{uu} = 0.9$, contour spacing 0.1, (b) R_{ww}, same contour levels as for R_{uu}, (c) $R_{\lambda u}$, contour level is 0 at centre of correlation, contour spacing 0.04, red positive, blue negative, (d) $R_{\lambda w}$, same contour levels as for $R_{\lambda u}$.

the results from the x–y plane measurements in figure 24. Spanwise cuts are shown in figure 32, showing negatively correlated regions that correspond to the oppositely signed u' streaks, on either side of the central peak. If the scale of the figure were increased, additional alternating positive and negative peaks would appear at larger $\Delta z/\delta$. This is shown in the $R_{\lambda u}$ contours of figure 31, which include as many as 8 low magnitude streamwise streaks of alternating sign extending across the entire measurement span. A spanwise length scale, Lz_{uu}, can be defined based on a particular contour or the distance from the central peak to the nearest negative peak. This was done for all cases, and the results were virtually identical to those of figure 30, since the LSE results and R_{uu} are based on the same data.

The R_{ww} correlation generally followed the same trends as R_{uu}, but like R_{vv} in the x–y plane, the changes were small relative to the scatter in the results. Contours of
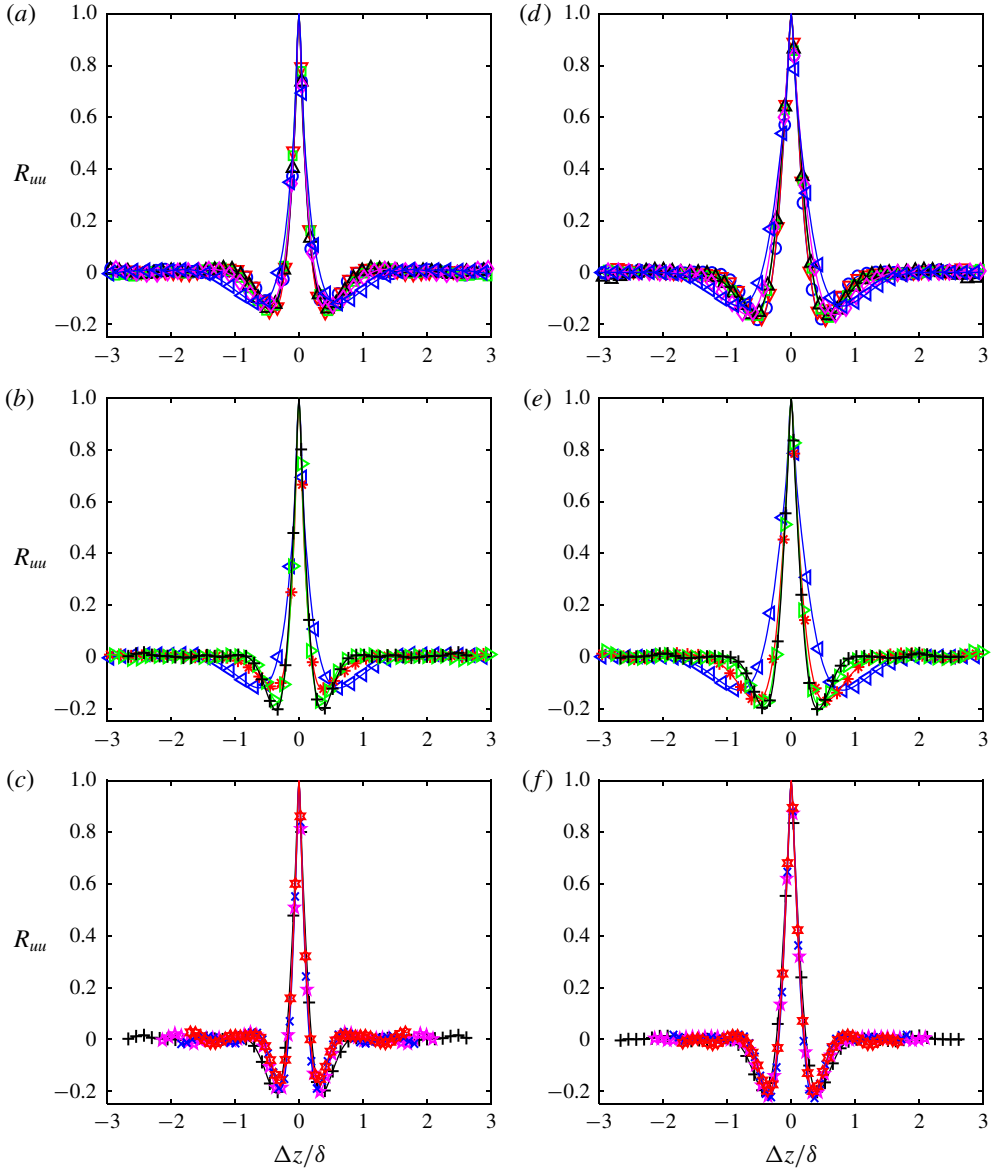
FIGURE 32. Spanwise slices through self-correlation point of R_{uu} of case 2, (*a*) centred at $y/\delta = 0.15$, St. 1–6, (*b*) $y/\delta = 0.15$, St. 6–9, (*c*) $y/\delta = 0.15$, St. 9–12, (*d*) $y/\delta = 0.4$, St. 1–6, (*e*) $y/\delta = 0.4$, St. 6–9, (*f*) $y/\delta = 0.4$, St. 9–12. Symbols from table 2.

the R_{uw} correlation are shown in figure 33. The same contour pattern was shown for ZPG boundary layers in Volino *et al.* (2007). The four peaks around the centre of the correlation correspond to the expected signs for u' and w' induced by the counter rotating hairpin vortex legs driving and on either side of a high or low speed streak. The structures increase in size in both the spanwise and streamwise directions in response to the FPG. This is followed by a rapid reversal in the recovery region and little change in the APG. The shape of the contours is different at $y/\delta = 0.15$ and 0.4.
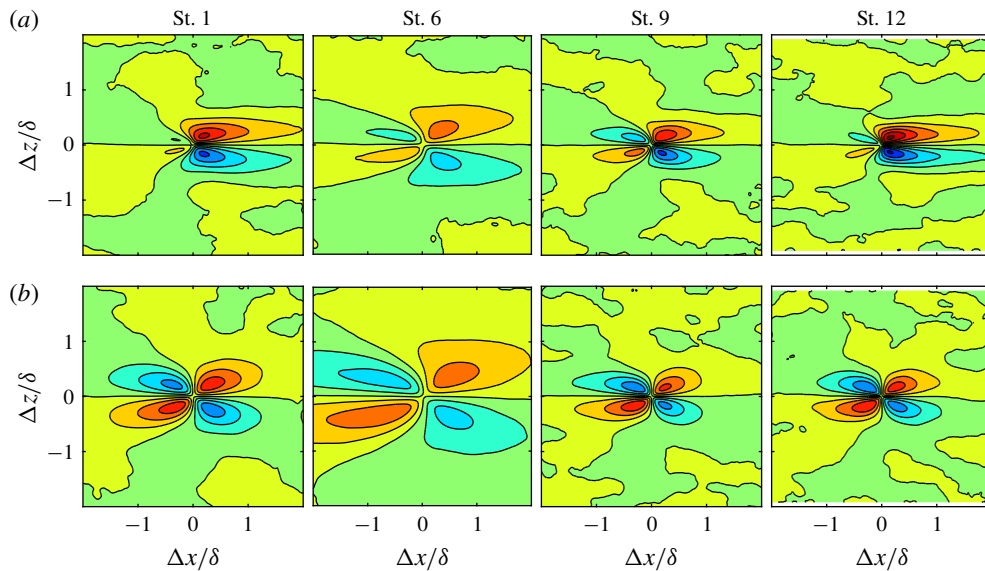
FIGURE 33. Contours of R_{uw} correlation for case 2, (*a*) $y/\delta = 0.15$, (*b*) $y/\delta = 0.4$. Contour level is 0 at centre of correlation, contour spacing 0.04, red positive, blue negative.

As noted by Ganapathisubramani, Longmire & Marusic (2006), this may be due to a different inclination angle of the vortex legs at different distances from the wall. Closer to the wall where the inclination angle is presumably smaller, there is more asymmetry between the upstream and downstream sides of the correlation. Farther from the wall, where the leg is presumably more vertical, there is more symmetry. The pressure gradient also has an effect on the asymmetry, and as noted above for the statistics and the structures in the *x*–*y* plane, the pressure gradient effect is stronger farther from the wall. At $y/\delta = 0.4$ in the FPG region, the peaks become more elongated in the streamwise direction on the upstream side of the correlation centre, while the peaks expand more equally in the streamwise and spanwise directions on the downstream side. The acceleration was shown above in figures 22, 23, 25 and 28 to reduce the inclination angle of structures with respect to the wall. A reduction of the average inclination angle of the hairpin legs may be responsible for the asymmetry in the same way the asymmetry at $y/\delta = 0.15$ was attributed to a lower angle. A reduction in the inclination angle of the hairpin and the accompanying elongation in the streamwise direction is consistent with the increasing streamwise scales of all quantities in the near-wall region in response to the FPG. The opposite is observed in the APG, where the streamwise symmetry increases. This is presumably due to the increased inclination angle observed in figure 25(*c*). The change is subtle, but was seen consistently in the ramp 1 and 2 cases. For the weaker pressure gradient of ramp 3, less change in the structure occurred. The locations of the peak magnitude in R_{uw} in each direction from the centre of the correlation are shown for all stations of case 2 in figure 34. At $y/\delta = 0.15$ there is no clear progression of the peaks in the streamwise direction, and the changes in the location are relatively small. This indicates that the size of the structure scales with δ. At $y/\delta = 0.4$ there is a clear progression away from the centre of the correlation in the FPG in both the streamwise and spanwise directions, with the streamwise increase noticeably larger
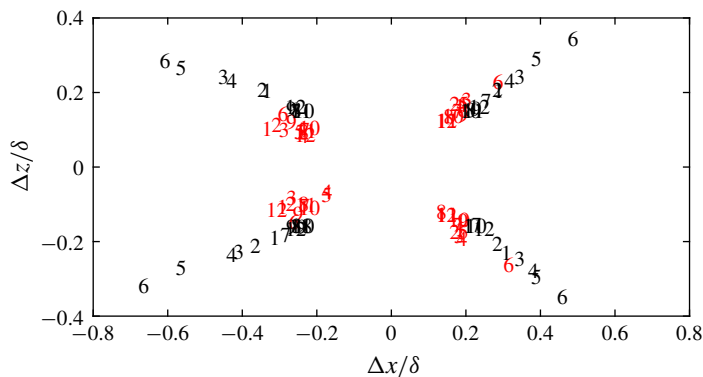
FIGURE 34. Location of peak magnitude of R_{uw} in each quadrant of x–z plane for case 2. Numbers plotted indicate streamwise station number. Red indicates $y/\delta = 0.15$, black $y/\delta = 0.4$.

than the spanwise. In the ZPG recovery, there is a rapid reversal of the growth and no distinguishable further change in the APG.

4. Conclusions

Experimental measurements have been presented from smooth-wall boundary layers to document the non-equilibrium response of the turbulence statistics and structure to changing pressure gradients. In each experimental case, the boundary layer was subject to a ZPG development region followed by a FPG with a constant K, a ZPG recovery region and an APG region with a constant K. Cases were documented over a range of Reynolds numbers and with K ranging from 0.125×10^{-6} to 2×10^{-6} in the FPG and from -0.0625×10^{-6} to -1×10^{-6} in the APG. Two component velocity profiles were acquired at 12 streamwise stations along the spanwise centreline of the test section. Velocity fields were acquired at the same streamwise stations using planar PIV in streamwise–wall-normal planes at the spanwise centreline and streamwise–spanwise planes at $y/\delta = 0.15$ and 0.4.

In defect coordinates, the mean streamwise velocity profile was lowered by the FPG toward a sink flow equilibrium. In cases with strong pressure gradients, there was an overshoot of the sink flow profile. In wall coordinates the wake was suppressed by the FPG and the profile rose above the canonical ZPG log law. In the ZPG recovery region, the boundary layer returned to canonical ZPG conditions. The APG caused a rise in the profile in defect coordinates and growth of the wake in wall coordinates. The differences between the measured profiles and canonical ZPG profiles at the same Reynolds numbers were shown as functions of streamwise location. A streamwise scaling based on the sink flow length was found for each flow region that collapsed the results for all cases of the present study. For the FPG, different collapses were found for results from the literature, indicating a dependence on initial conditions.

The inner peak in the streamwise component of the Reynolds stress scaled with the wall shear and was largely unchanged in magnitude and location at $y^+ = 15$ in the FPG and ZPG recovery regions. It exhibited growth in the APG when scaled with the friction velocity, but remained at $y^+ = 15$. Farther from the wall, in both inner and outer scaling, all the Reynolds stresses were suppressed by the FPG, rapidly returned to canonical ZPG conditions in the recovery region, and grew in the APG.

The locations of the inner region peaks in the Reynolds stresses and higher-order quantities did not vary significantly with pressure gradient when expressed in terms of y^+. Similarly, the location of the outer region peaks tended to remain at fixed locations when expressed in terms of y/δ. Quadrant analysis of the Reynolds shear stress showed a rise in the importance of ejections relative to sweeps in the FPG region due to straining of the turbulence in the outer part of the boundary layer and a subsequent reduction of the contribution from the sweeps. This was followed by a return to ZPG conditions in the recovery and a reversal in the APG, where the drop in the wall shear caused a reduction in the contribution from ejections. For all of these changes in the Reynolds stresses, the differences from the canonical ZPG case were shown as a function of streamwise location, and as with the mean velocity, a scaling was found for each region to collapse the results. Spectra of the Reynolds stresses increased and decreased in magnitude in response to pressure gradient changes, but wavenumbers were largely invariant when inner scaling was used for v'^2, and mixed scaling was used for u'^2 and $u'v'$. Triple products of the fluctuating velocity components were shown and explained in terms of the wall-normal transport of the Reynolds stresses. The changes with pressure gradient of the location and magnitude of each peak in the profiles were related to the behaviour of the corresponding peaks in the Reynolds stresses. The largest production terms in the budget equations of the Reynolds stresses were also examined, and differences from the canonical ZPG case were shown as a function of streamwise location. The same scaling used with other turbulence quantities was found to collapse the results in each region of the flow.

The turbulence structure was examined using linear stochastic estimation and two point correlations of the PIV data. Structures increased in size relative to the boundary layer thickness in both the streamwise and spanwise directions in the FPG region, and quickly returned to their original size in the ZPG recovery. The increase in streamwise length in the FPG was particularly apparent close to the wall. Changes were smaller in the APG region, indicating that the structures grew at the same rate as the boundary layer thickness. In all regions, there was little change in the wall-normal extent of the correlations relative to δ. Lengths and inclination angles of turbulent structures were quantified and shown as functions of streamwise location. Using the same streamwise scaling as with other quantities, the results from all cases were again collapsed in each flow region.

The present results describe a particular type of pressure gradient involving fully developed, canonical turbulent ZPG boundary layers that are then subject to an FPG with constant K acceleration (sink flows moving toward equilibrium) or constant K deceleration (non-equilibrium with continuously increasing β). The β values ranged from -1 to 6 in the various cases, and the Re_θ range was about 700–7000 ($300 < Re_\tau < 1900$). Some similarities to other pressure gradients (e.g. equilibrium APG cases) have been shown, but differences from cases with other upstream conditions or pressure gradient histories have also been noted. The scalings and descriptions presented above appear to be useful for a range of flows of interest, but not necessarily universal for all arbitrary pressure gradients or at higher Reynolds numbers.
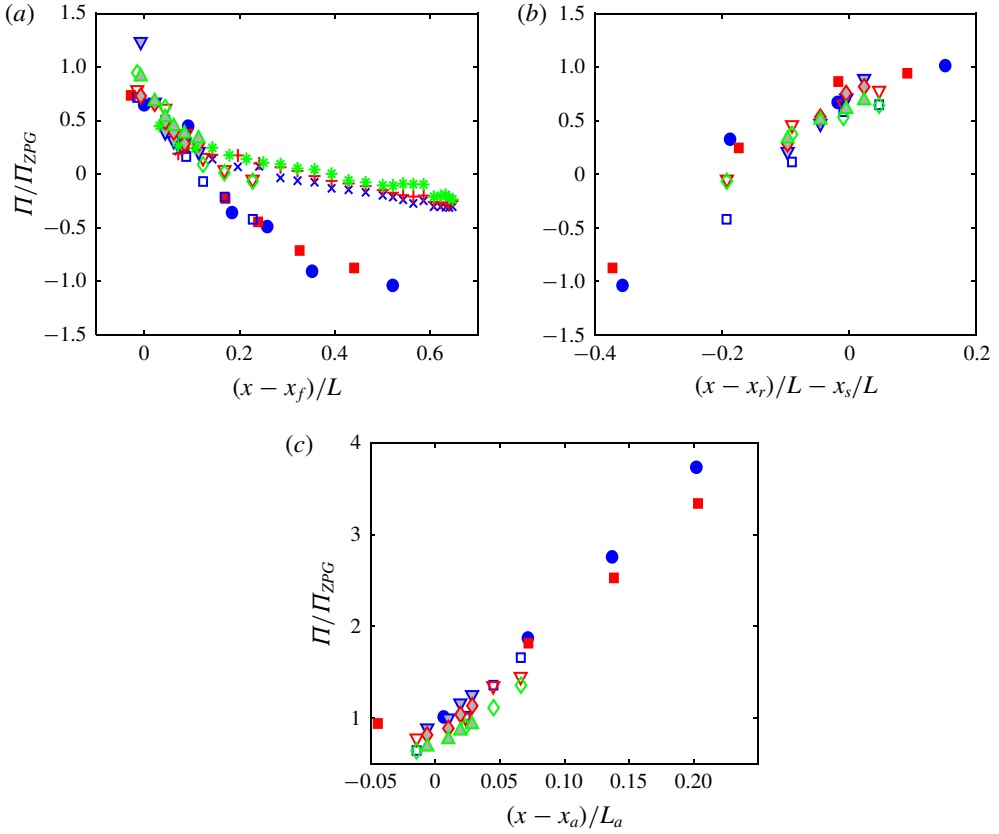
Acknowledgements

FIGURE 35. Wake strength normalized on ZPG wake strength at same Re_θ (*a*) FPG St. 1–6, (*b*) ZPG St. 6–9, (*c*) APG St. 9–12. Symbols from table 1 for cases of present study. Symbols for Jones (1998) results: ×, $K = 0.539 \times 10^{-6}$; +, $K = 0.359 \times 10^{-6}$; *, $K = 0.270 \times 10^{-6}$.

Declaration of interests

The authors report no conflict of interest.

Appendix

A few additional quantities that are helpful for understanding the boundary layer development are considered here, beginning with quantities determined from the mean velocity profiles. The wake strength was defined in (2.3), and its suppression by the FPG and rapid growth in the APG were shown in figure 2. Its streamwise development is shown in figure 35 using the format of figure 3. The wake strength is normalized using the corresponding value for the canonical ZPG case at the same Re_θ. In the FPG region, the wake strength drops rapidly at first. The cases that proceed farther toward L appear to approach an equilibrium value, which is lower for the cases with higher K. In figure 35(*b*), the data for all cases collapse onto the same curve, and reach canonical ZPG values by the end of the recovery. Similar collapse is observed in the APG region.
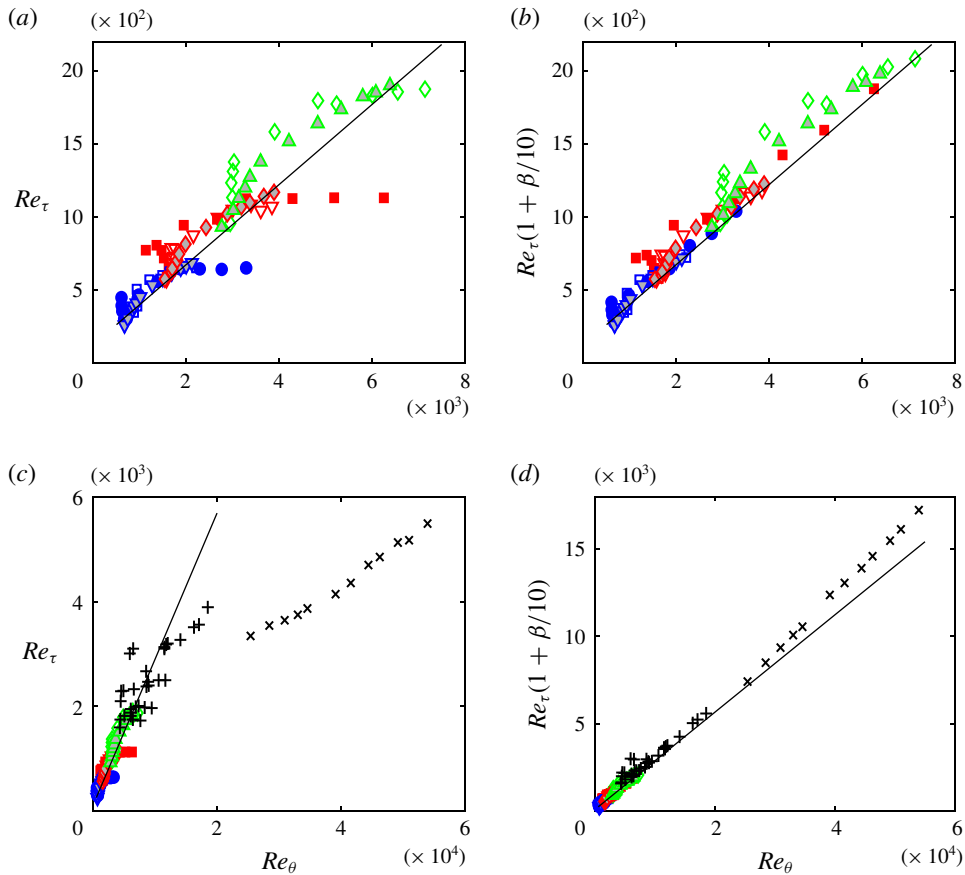
FIGURE 36. Friction Reynolds versus Re_θ. Symbols for present cases from table 1. Solid line is fit to ZPG result from Volino (2020). (*a*) Present study, uncorrected (*b*) presented study with $(1 + \beta/10)$ correction, (*c*) uncorrected and including results of Harun *et al.* (2013) (+) and Skåre & Krogstad (1994) (×), (*d*) corrected with $(1 + \beta/10)$ and including Harun *et al.* (2013) and Skåre & Krogstad (1994) results.

In a canonical ZPG boundary layer, Re_τ varies linearly with Re_θ, as observed in the DNS results of Jiménez *et al.* (2010) and Sillero *et al.* (2013), and shown in Volino (2020). As shown in table 1 and figure 36(*a*), Re_τ grew even as Re_θ was decreasing with a FPG, and in the APG, Re_τ remained nearly constant in the ramp 1 and 2 cases while Re_θ was growing rapidly. The FPG suppresses the growth of both δ and θ, and the thinner boundary layer increases the wall shear, causing u_τ to rise relative to U_∞. This results in Re_τ increasing more rapidly relative to Re_θ than in the ZPG. In the APG the effect is opposite, and more pronounced, as both δ and θ increase rapidly, and the thicker boundary layer reduces the wall shear, causing u_τ to drop relative to U_∞. The change in Re_τ behaviour must be some function of the pressure gradient, and a simple relationship would be a linear function of β. If Re_τ is multiplied by a correction factor of $(1 + \beta/10)$, the data agree better with the ZPG result, as shown in figure 36(*b*). The correction does little in the FPG where β is small and the data rise above the ZPG line, but has a significant effect in the APG. The data of Skåre & Krogstad (1994) and Harun *et al.* (2013) are added in figure 36(*c*,*d*) for comparison.
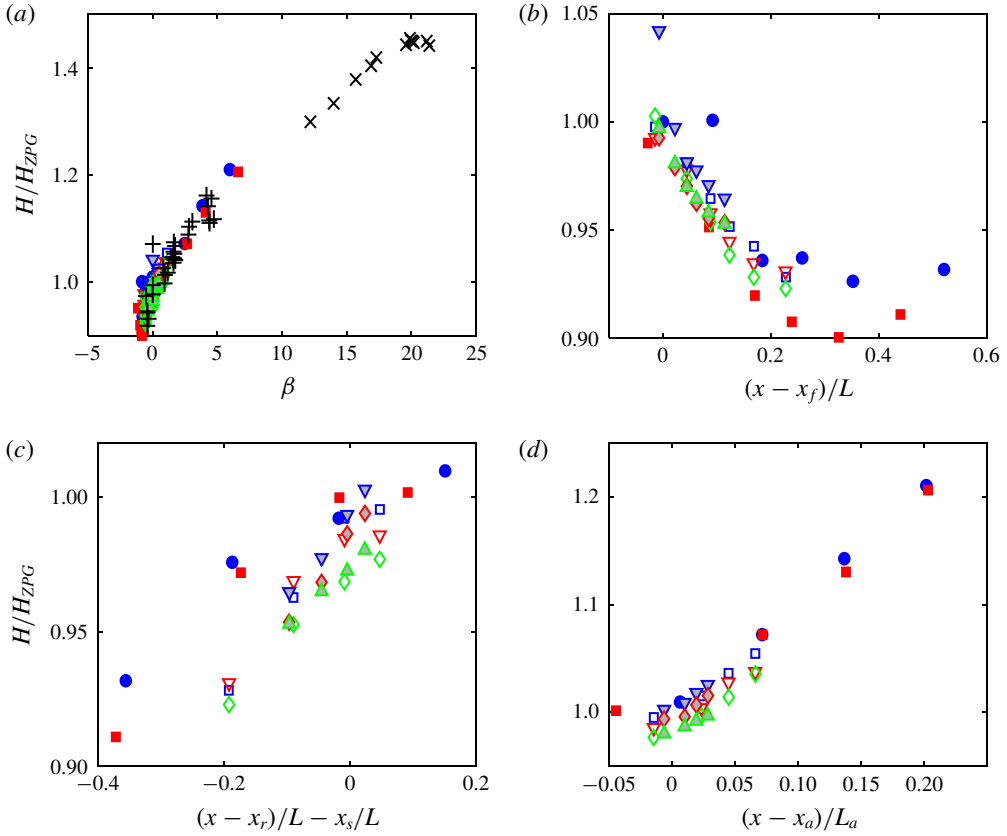
FIGURE 37. Shape factor, H, normalized on H for ZPG case at same Re_θ (a) as function of β, (b) FPG St. 1–6, (c) ZPG St. 6–9, (d) APG St. 9–12. Symbols for present cases from table 1, + for Harun *et al.* (2013), × for Skåre & Krogstad (1994).

Without correction, there is considerable variation between cases, but the $(1 + \beta/10)$ multiplier again collapses the data onto a single curve. The results agree with the ZPG fit of Volino (2020) to approximately $Re_\theta = 25\,000$, beyond which the slope increases. This increase in slope is consistent with the high Reynolds number ZPG results of Vincenti *et al.* (2013). The linear form of the correction and the constant 10 were determined empirically, but the trend of the correction is expected, as explained above. It applies to the cases in figure 36, which are near equilibrium or have monotonically increasing β. It did not agree with data from cases with different pressure gradient histories, such as those presented in Bobke *et al.* (2017).

The shape factor, $H = \delta^*/\theta$, provides another quantification of the development of the boundary layer. Figure 37(a) shows H for each profile normalized on the corresponding H for the canonical ZPG case at the same Re_θ, plotted as a function of β. All cases appear to follow the same curve of increasing H with β, including those of Harun *et al.* (2013) and Skåre & Krogstad (1994). The streamwise development of H is shown in figure 37(b–d) in the coordinates of figure 3. The ratio H/H_{ZPG} appears to asymptote to a value of about 0.92 if given long enough to develop in the FPG region. The common asymptote for all cases is consistent
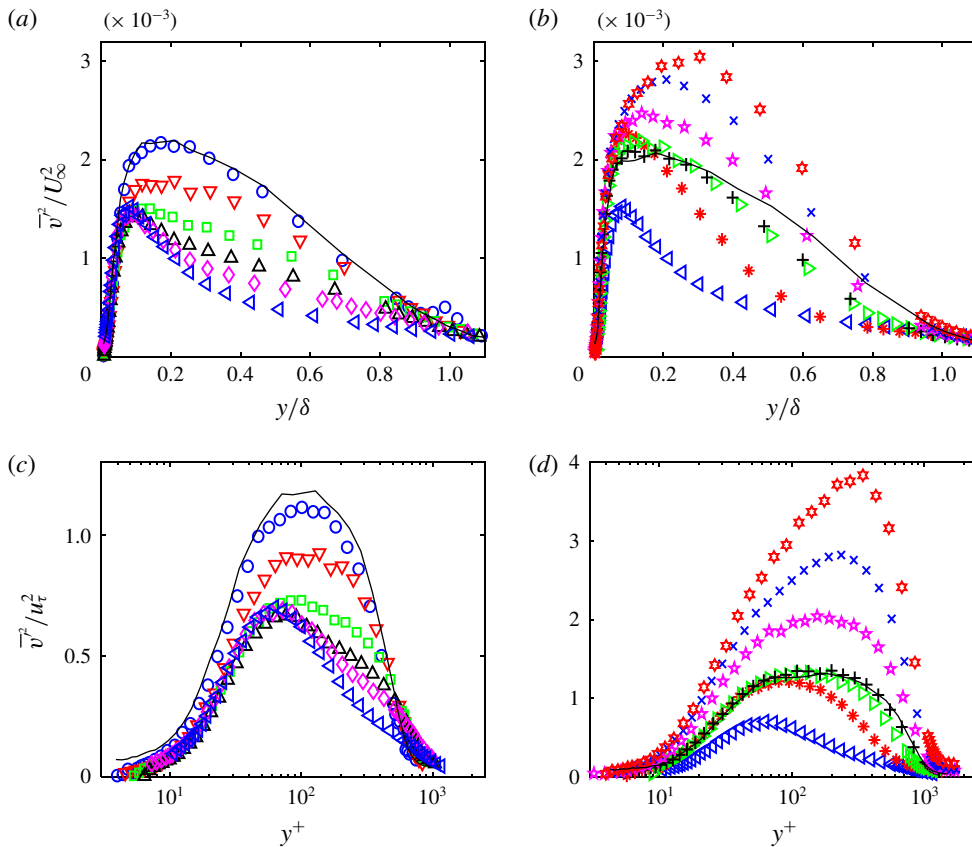
FIGURE 38. Wall-normal Reynolds normal stress profiles for case 2, (*a*) outer scaling for St. 1–6, (*b*) outer scaling for St. 6–12, (*c*) inner scaling for St. 1–6, (*d*) inner scaling for St. 6–12. Symbols from table 2. Lines: —— canonical ZPG comparison.

with the common sink flow profile in defect coordinates noted in §3.1. The ratio in all cases returns to 1 in the recovery, and then rises in the APG. Figures 37(*a*) and 37(*d*) convey the same information since β was shown to be a function of streamwise location in figure 5(*a*).

Considering turbulence quantities next, the $\overline{v'^2}$ profiles for case 2 are shown in figure 38, and the streamwise development for all cases is shown in figure 39 in the format of figure 8. The behaviour is virtually identical to that of $-\overline{u'v'}$ in figures 10 and 11. The triple products also show great similarity to quantities above. Profiles of $\overline{u'^2 v'}$ are shown in figure 40 for case 2. The locations of the peaks and their response to the pressure gradient are the same as shown for $\overline{u'^3}$ in figure 14. The signs of the $\overline{u'^3}$ and $\overline{u'^2 v'}$ peaks are opposite since u' and v' have opposite signs in Q2 and Q4 events, and $\overline{u'^3}$ has larger magnitude than $\overline{u'^2 v'}$ since the average fluctuations in u' are larger than in v'. Otherwise, both quantities result from wall-normal transport of $\overline{u'^2}$ by ejections and sweeps and can be similarly explained. The same relationship exists between $\overline{u'v'^2}$ of figure 41 and $\overline{v'^3}$ of figure 16. Both result from wall-normal transport of $\overline{v'^2}$.
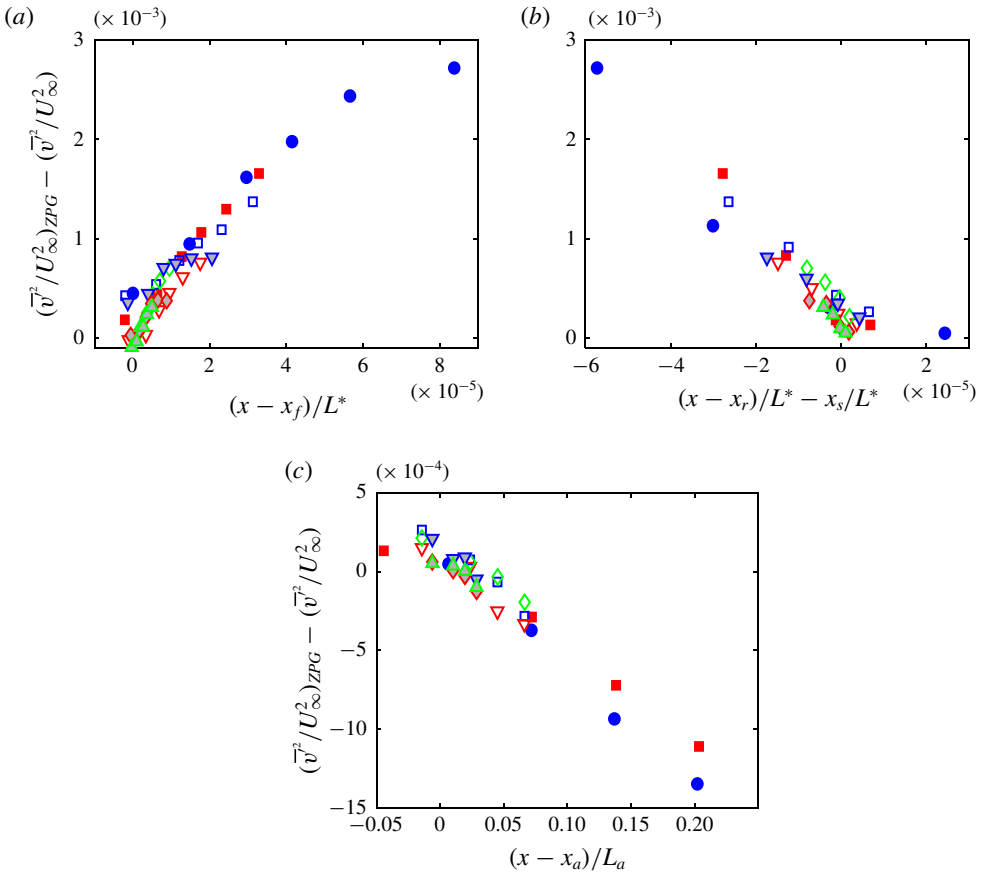
FIGURE 39. Difference between ZPG and non-ZPG $\overline{v'^2}/U_\infty^2$ profiles at $y/\delta = 0.4$. ZPG and non-ZPG compared at same Re_θ. (*a*) FPG St. 1–6, (*b*) ZPG St. 6–9, (*c*) APG St. 9–12. Symbols from table 1.
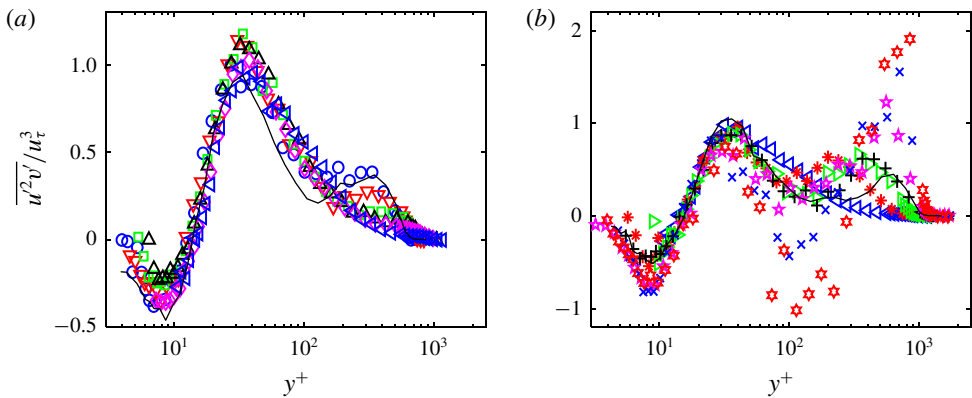

FIGURE 40. The $\overline{u'^2 v'}$ profiles for case 2, (*a*) St. 1–6, (*b*) St. 6–12. Symbols from table 2. Lines: —— canonical ZPG comparison.
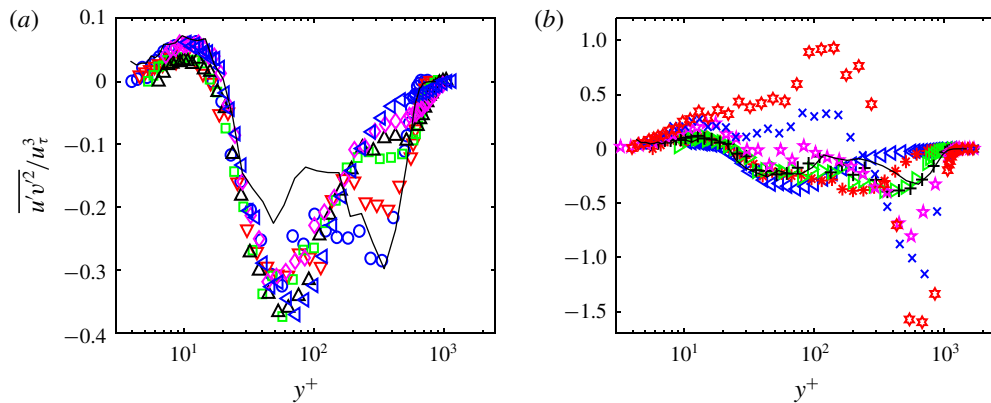
FIGURE 41. The $\overline{u'v'^2}$ profiles for case 2, (*a*) St. 1–6, (*b*) St. 6–12. Symbols from table 2. Lines: —— canonical ZPG comparison.

REFERENCES

ADRIAN, R. J., MEINHART, C. D. & TOMKINS, C. D. 2000 Vortex organization in the outer region of the turbulent boundary layer. *J. Fluid Mech.* **422**, 1–54.

ADRIAN, R. J. & MOIN, P. 1988 Stochastic estimation of organized turbulent structure – homogeneous shear-flow. *J. Fluid Mech.* **190**, 531–559.

AUBERTINE, C. D. & EATON, J. K. 2005 Turbulence development in a non-equilibrium turbulent boundary layer with mild adverse pressure gradient. *J. Fluid Mech.* **532**, 345–364.

BOBKE, A., VINUESA, R., ORLU, R. & SCHLATTER, P. 2017 History effects and near equilibrium in adverse-pressure-gradient turbulent boundary layers. *J. Fluid Mech.* **820**, 667–692.

BRADSHAW, P. 1967 Inactive motion and pressure fluctuations in turbulent boundary layers. *J. Fluid Mech.* **30**, 241–258.

CASTILLO, L. & GEORGE, W. K. 2001 Similarity analysis for turbulent boundary layer with pressure gradient: outer flow. *AIAA J.* **39**, 41–47.

CHIEN, K.-Y. 1982 Prediction of channel and boundary-layer flows with a low-Reynolds-number turbulence model. *AIAA J.* **20**, 32–38.

CHRISTENSEN, K. T. & ADRIAN, R. J. 2001 Statistical evidence of hairpin vortex packets in wall turbulence. *J. Fluid Mech.* **431**, 433–443.

CHRISTENSEN, K. T. & WU, Y. 2005 Characteristics of vortex organization in the outer layer of wall turbulence. In *Proceedings of the Fourth International Symposium on Turbulence and Shear Flow Phenomena, Williamsburg, Virginia*, vol. 3, pp. 1025–1030. TSFP.

CRAWFORD, M. E. & KAYS, W. M. 1976 STAN5 – a program for numerical computation of two-dimensional internal and external boundary layer flows. NASA CR 2742.

DEGRAAFF, D. B. & EATON, J. K. 2000 Reynolds-number scaling of the flat-plate turbulent boundary layer. *J. Fluid Mech.* **422**, 319–346.

FERNHOLZ, H. H. & FINLEY, P. J. 1996 The incompressible zero-pressure-gradient turbulent boundary layer: an assessment of the data. *Prog. Aerosp. Sci.* **32**, 245–311.

GANAPATHISUBRAMANI, B., LONGMIRE, E. & MARUSIC, I. 2006 Experimental investigation of vortex properties in a turbulent boundary layer. *Phys. Fluids* **18**, 055105.

HAMBLETON, W. T., HUTCHINS, N. & MARUSIC, I. 2006 Simultaneous orthogonal-plane particle image velocimetry measurements in a turbulent boundary layer. *J. Fluid Mech.* **560**, 53–64.

HARUN, Z., MONTY, J. P., MATHIS, R. & MARUSIC, I. 2013 Pressure gradient effects on the large-scale structure of turbulent boundary layers. *J. Fluid Mech.* **715**, 477–498.

HUTCHINS, N., HAMBLETON, W. T. & MARUSIC, I. 2005 Inclined cross-stream stereo particle image velocimetry measurements in turbulent boundary layers. *J. Fluid Mech.* **541**, 21–54.

JIMÉNEZ, J., HOYAS, S., SIMENS, M. P. & MIZUNO, Y. 2010 Turbulent boundary layers and channels at moderate Reynolds numbers. *J. Fluid Mech.* **657**, 335–360.

JONES, M. B. 1998 Evolution and structure of sink flow turbulent boundary layers. PhD thesis, University of Melbourne.

JONES, M. B., MARUSIC, I. & PERRY, A. E. 2001 Evolution and structure of sink-flow turbulent boundary layers. *J. Fluid Mech.* **428**, 1–27.

KAYS, W. M. & CRAWFORD, M. E. 1980 *Convective Heat and Mass Transfer*, 2nd edn. McGraw-Hill.

KITSIOS, V., SEKIMOTO, A., ATKINSON, C., SILLERO, J. A., BORRELL, G., GUNGOR, A. G., JIMÉNEZ, J. & SORIA, J. 2017 Direct numerical simulation of a self-similar adverse pressure gradient turbulent boundary layer at the verge of separation. *J. Fluid Mech.* **829**, 392–419.

KLEWICKI, J. C. 2010 Reynolds number dependence, scaling, and dynamics of turbulent boundary layers. *Trans. ASME J. Fluids Engng* **132**, 094001.

LEE, J. H. 2017 Large-scale motions in turbulent boundary layers subjected to adverse pressure gradients. *J. Fluid Mech.* **810**, 323–361.

LEE, J.-H. & SUNG, H. J. 2009 Structures in turbulent boundary layers subjected to adverse pressure gradients. *J. Fluid Mech.* **639**, 101–131.

MELLOR, G. L. & GIBSON, D. M. 1966 Equilibrium turbulent boundary layers. *J. Fluid Mech.* **24**, 225–253.

MONTY, J. P., HARUN, Z. & MARUSIC, I. 2011 A parametric study of adverse pressure gradient turbulent boundary layers. *Intl J. Heat Fluid Flow* **32**, 575–585.

NAGIB, H. M., CHAUHAN, K. A. & MONKEWITZ, P. A. 2007 Approach to an asymptotic state for zero pressure gradient turbulent boundary layers. *Phil. Trans. R. Soc. Lond.* A **365**, 755–770.

REYNOLDS, W. C. 1976 Computation of turbulent flows. *Annu. Rev. Fluid Mech.* **8**, 183–208.

SAMIE, M., MARUSIC, I., HUTCHINS, N., FU, M. K., FAN, Y., HULTMARK, M. & SMITES, A. J. 2018 Fully resolved measurements of turbulent boundary layer flows up to $Re_\tau = 20\,000$. *J. Fluid Mech.* **851**, 391–415.

SILLERO, J. A., JIMÉNEZ, J. & MOSER, R. D. 2013 One-point statistics for turbulent wall-bounded flows at Reynolds numbers up to $\delta^+ \approx 2000$. *Phys. Fluids* **25**, 105105.

SKÅRE, P. R. & KROGSTAD, P.-Å. 1994 A turbulent equilibrium boundary layer near separation. *J. Fluid Mech.* **532**, 319–348.

SKOTE, M., HENNINGSON, D. S. & HENKES, R. A. W. M. 1998 Direct numerical simulation of self-similar turbulent boundary layers in adverse pressure gradients. *Flow Turbul. Combust.* **60**, 47–85.

SPALART, P. R. 1986 Numerical study of sink-flow boundary layers. *J. Fluid Mech.* **172**, 307–328.

VINCENTI, P., KLEWICKI, J., MORRILL-WINTER, C., WHITE, C. M. & WOSNIAK, M. 2013 Streamwise velocity statistics in turbulent boundary layers that spatially develop to high Reynolds numbers. *Exp. Fluids* **54**, 1629.

VOLINO, R. J. 2020 Reynolds number dependence of zero pressure gradient turbulent boundary layers. *Trans. ASME J. Fluids Engng* **142**, 051303.

VOLINO, R. J. & SCHULTZ, M. P. 2018 Determination of wall shear stress from mean velocity and Reynolds shear stress profiles. *Phys. Rev. Fluids* **3**, 034606.

VOLINO, R. J., SCHULTZ, M. P. & FLACK, K. A. 2007 Turbulence structure in rough- and smooth-wall boundary layers. *J. Fluid Mech.* **592**, 263–293.

VOLINO, R. J., SCHULTZ, M. P. & FLACK, K. A. 2009 Turbulence structure in boundary layers with two-dimensional roughness. *J. Fluid Mech.* **635**, 75–101.

WEI, T., FIFE, P., KLEWICKI, J. & MCMURTRY, P. 2005 Properties of the mean momentum balance in turbulent boundary layer, pipe and channel flows. *J. Fluid Mech.* **522**, 303–327.

WILLMARTH, W. W. & LU, S. S. 1972 Structure of the Reynolds stress near the wall. *J. Fluid Mech.* **55**, 65–92.

WU, Y. & CHRISTENSEN, K. T. 2006 Population trends of spanwise vortices in wall turbulence. *J. Fluid Mech.* **568**, 55–76.

ZHOU, J., ADRIAN, R. J., BALACHANDAR, S. & KENDALL, T. M. 1999 Mechanisms for generating coherent packets of hairpin vortices in channel flow. *J. Fluid Mech.* **387**, 353–396.